1   **Rhinovirus C replication is associated with the endoplasmic reticulum and triggers**

2   **cytopathic effects in an *in vitro* model of human airway epithelium**

3

4   Talita B. Gagliardi[1], Monty E. Goldstein[1], Daniel Song[2], Kelsey M. Gray[2], Jae W. Jung[2], Kimberly

5   M. Stroka[2,3,4,5], Gregg A. Duncan[2], and Margaret A. Scull[1,#]

6

7   [1] Department of Cell Biology and Molecular Genetics, Maryland Pathogen Research Institute,

8   University of Maryland, College Park, MD 20742, USA

9   [2] Fischell Department of Bioengineering, University of Maryland, College Park, MD 20742, USA

10   [3] Biophysics Program, University of Maryland, College Park, MD 20742, USA

11   [4] Center for Stem Cell Biology and Regenerative Medicine, University of Maryland – Baltimore,

12   MD, 21201, USA

13   [5] Marlene and Stewart Greenebaum Comprehensive Cancer Center, University of Maryland –

14   Baltimore, MD 21201, USA

15   [#] Corresponding author: scull@umd.edu

16

17   **Running Title:** Rhinovirus C replication in human airway epithelium

18

19   **Keywords:** rhinovirus C; microscopy; single-cell analysis; epithelial integrity; viral replication

20

21

22

23

24

25

Abstract

The clinical impact of rhinovirus C (RV-C) is well-documented; yet the viral life cycle remains poorly defined. Thus, we characterized RV-C15 replication at the single-cell level and its impact on the human airway epithelium (HAE) using a physiologically-relevant *in vitro* model. RV-C15 replication was restricted to ciliated cells where viral RNA levels peaked at 12 hours post-infection (hpi), correlating with elevated titers in the apical compartment at 24 hpi. Notably, infection was associated with a loss of polarized expression of the RV-C receptor, cadherin-related family member 3. Visualization of double-stranded RNA (dsRNA) during RV-C15 replication revealed two distinct replication complex arrangements within the cell, likely corresponding to different time points in infection and correlating with the formation of large intracellular vesicles. To further define RV-C15 replication sites, we analyzed the expression of giantin, phosphatidylinositol-4-phosphate, and calnexin, as well as the colocalization of these markers with dsRNA. Fluorescence levels of all three cellular markers were elevated during infection and altered giantin distribution further indicated Golgi fragmentation. However, unlike previously characterized RVs, the high ratio of calnexin-dsRNA colocalization implicated the endoplasmic reticulum as the primary site for RV-C15 replication in HAE. RV-C15 infection was also associated with elevated stimulator of interferon genes (STING) expression, facilitating replication, and the induction of incomplete autophagy, a mechanism used by other RVs to promote non-lytic release of progeny virions. Finally, RV-C15 infection resulted in a temporary loss in epithelial barrier integrity and the translocation of tight junction proteins while a reduction in mucociliary clearance indicated cytopathic effects on epithelial function. Together, our findings identify both shared and unique features of RV-C replication compared to related rhinoviruses and define the impact of RV-C on both epithelial cell organization and tissue functionality – aspects of infection that may contribute to pathogenesis *in vivo*.

Author summary

Rhinovirus C has a global distribution and significant clinical impact – especially in those with underlying lung disease. Although RV-C is genetically, structurally, and biologically distinct from RV-A and -B viruses, our understanding of the RV-C life cycle has been largely inferred from these and other related viruses. Here, we performed a detailed analysis of RV-C15 replication in a physiologically-relevant model of human airway epithelium. Our single-cell, microscopy-based approach revealed that – unlike other RVs – the endoplasmic reticulum is the primary site for RV-C15 replication. RV-C15 replication also stimulated STING expression, which was proviral, and triggered dramatic changes in cellular organization, including altered virus receptor distribution, fragmented Golgi stacks, and the induction of incomplete autophagy. Additionally, we observed a loss of epithelial barrier function and a decrease in mucociliary clearance, a major defense mechanism in the lung, during RV-C15 infection. Together, these data reveal novel insight into RV-C15 replication dynamics and resulting cytopathic effects in the primary target cells for infection, thereby furthering our understanding of the pathogenesis of RV-C. Our work highlights similar, as well as unique, aspects of RV-C15 replication compared to related pathogens, which will help guide future studies on the molecular mechanisms of RV-C infection.

Introduction

Rhinoviruses (RVs) are responsible for over 40% of respiratory virus infections in the human population [1-4]. Although well known as etiologic agents of the common cold, rhinoviruses can also infect the lower respiratory tract causing bronchiolitis or pneumonia and are a leading cause of virus-induced exacerbations in acute and chronic lung disease [5-8]. No vaccine or direct-acting antiviral is currently available due in part to the diversity of RVs in circulation, with over 160 genotypes identified [9-10]. These genotypes comprise three species (RV-A, RV-B, and RV-C) where RV-A and RV-C are the most prevalent and RV-C is associated with more severe

3

76   clinical disease, especially in children [4, 11, 12]. Indeed, RV infection during the first year of life

77   has been associated with wheezing episodes and is considered a risk factor for the development

78   of asthma [8, 13, 14].

79   RV-C was discovered in 2006 [15] and compared to previously defined rhinovirus species,

80   is unique at the genetic [16], structural [17], and biological level [18]. While all RVs (-A, -B, and -

81   C) infect airway epithelial cells, RV-C uses a different host protein, cadherin-related family

82   member 3 (CDHR3), to mediate particle uptake [19]. The restricted expression of CDHR3 to

83   ciliated cells in the upper and lower airway epithelium [20-23] limits the cellular tropism of RV-C,

84   compared to other RVs that utilize low-density lipoprotein receptor (LDLR) or intercellular

85   adhesion molecule (ICAM)-1 as receptors [18]. Notably, a non-synonymous single nucleotide

86   polymorphism (SNP; rs6967330[A]) that yields stabilized CDHR3 protein expression at the cell

87   surface is a causal variant for early childhood asthma with severe exacerbations [20]. Subsequent

88   investigation has associated the CDHR3 asthma risk allele with heightened risk of respiratory

89   tract illness with RV-C, but not other viruses [21]. More recently, stimulator of interferon genes

90   (STING), a key adapter protein for cytosolic DNA-sensing pathways, was found to play a proviral

91   role in RV-A and -C, but not -B, replication [24]. Thus, mechanisms of infection and replication

92   are not always conserved between rhinovirus species.

93   Despite these advances, details of the RV-C life cycle and underlying mechanisms that

94   contribute to pathogenesis remain scarce. While such studies remain hampered by the absence

95   of immortalized cell lines or an *in vivo* mouse model that is naturally susceptible and highly

96   permissive for RV-C replication, previous reports demonstrate that *ex vivo* tissue and primary

97   airway cultures support infection [22, 25]. Nonetheless, aside from receptor usage and cellular

98   tropism, little is known about RV-C interactions with primary airway epithelial cells, the principal

99   target for infection. Here we utilized both single-cell, microscopy-based analyses, and culture-

100   wide measurements, to investigate the details of RV-C15 replication in an *in vitro* model of human

101   airway epithelium (HAE). Our data identify the endoplasmic reticulum (ER) as the primary site for

102   RV-C15 replication and demonstrate the impact of infection on the structural integrity of ciliated

103   cells and epithelial barrier function, thereby identifying both unique and shared features of RV-C

104   amongst related viruses.

105

Results

107   **1. RV-C15 replicates in ciliated cells, yielding changes in CDHR3 expression.**

108   Pseudostratified models of HAE at air-liquid interface are permissive for RV-C replication

109   [25, 26]. To detail the kinetics of RV-C15 replication in this model at higher-resolution, we

110   inoculated HAE at 34°C with 10^{10} RV-C15 RNA copies and quantified viral RNA intracellularly as

111   well as in both the apical and basolateral compartments over time (**Fig 1A and 1B**). The dynamics

112   of RV-C15 replication were similar in HAE from two different donors, where cell-associated RV-

113   C15 RNA levels increased during the first 12 hours post-infection (hpi). This correlated with the

114   detection of double-stranded (ds) RNA, a marker of viral replication, by immunofluorescence (IF;

115   **S1A Fig**) and was in line with peak viral release into the apical chamber at 24 hpi (**Fig 1A and**

116   **1B**). The lack of RV-C15 RNA in basolateral supernatants confirmed polarized release of RV-C15

117   to the airway lumen (**Fig 1A and 1B**), consistent with a previous report in nasal cells [27] and the

118   clinical manifestation of RV-C-mediated disease.

119   Given that HAE cultures were permissive for RV-C15 replication, we next sought to

120   investigate cell tropism in our system. Visualization of the RV-C receptor, CDHR3, in non-infected

121   HAE by IF revealed expression at the apical surface in cells that were also positive for Forkhead

122   box protein J1 (FoxJ1; known to promote ciliogenesis) or acetylated alpha-tubulin (a marker of

123   mature ciliated cells; **Fig 1C, 1D, and 1E**). Notably, the corrected total cellular fluorescence

124   (CTCF) levels of CDHR3 had a limited relationship with FoxJ1 but were strongly correlated with

125   acetylated alpha-tubulin levels, in line with increased expression of CDHR3 during differentiation

126   (**S1B and S1C Fig)** [21]. Corroborating these data and previous research reporting ciliated cell

127 tropism for RV-C [22, 25], we detected dsRNA primarily in FoxJ1(+) cells, with some cells also

128 staining positive for acetylated alpha-tubulin (**Fig 1F and S1D Fig**). However, the visibility of the

129 cilia in these cells was diminished (**Fig 1F**) and the 3D view suggested CDHR3 was internalized

130 in some dsRNA(+) cells, together with a more diffuse distribution of acetylated alpha-tubulin and

131 FoxJ1 (**Fig 1D and 1E**).

132   To better understand the dynamics of FoxJ1, acetylated alpha-tubulin, and CDHR3 during

133 infection, we analyzed global protein expression by Western blot (WB) and quantified

134 fluorescence levels following immunostaining specifically in infected cells. Beyond the intrinsic

135 variation expected across cultures in this model system, neither FoxJ1 nor acetylated alpha-

136 tubulin protein levels were dramatically altered over the course of infection while CDHR3 levels

137 fluctuated (**S1E, S1F Fig**). Subsequent single-cell analysis of acetylated alpha-tubulin and FoxJ1

138 fluorescence levels corroborated our WB data (**S1G, S1H Fig**); however, in contrast to the global

139 elevation of CDHR3 protein in RV-C15-infected HAE at 12 hpi, CDHR3 fluorescence levels

140 decreased significantly in cells with active viral replication (**Fig 1G**).

141

142 **2. RV replication complex distribution is associated with vesicle formation.**

143   Picornaviruses, including RV-A and -B, replicate in association with cellular membranes,

144 leading to the formation of double-membrane vesicles known as replicative complexes [28-31].

145 Thus, we investigated the distribution of replication complexes in RV-C15-infected HAE cultures

146 by visualization of viral dsRNA and the impact of infection on intracellular membrane organization

147 by transmission electron microscopy (TEM). While non-infected HAE were negative for dsRNA,

148 as expected (**Fig 2A**), dsRNA in RV-C15-infected cultures was found in either a perinuclear (**Fig**

149 **2B**) or "ring-like" disposition closer to apical and basolateral membranes (**Fig 2C**). Neither

150 phenotype was specific for RV-C15, however, as HAE infected with either RV-A16 or RV-A2

151 revealed similar dsRNA profiles (**S2A-D Fig**). Notably, the nuclei in cells with the "ring-like" dsRNA

152 pattern were found near the apical cell surface instead of the usual basolateral location in

6

153   polarized columnar cells (**Fig 2C, S2B, S2D Fig**), possibly a result of large intracellular vesicle

154   formation (**S2E and S2F Fig**).

155   Subsequent TEM analysis in non-infected HAE revealed a differentiated epithelium with

156   no overt cytopathic effects (**Fig 2D – left panel**) and a limited number of vacuoles in the cytoplasm

157   (**Fig 2D- right panel**). In contrast, in RV-C15-infected HAE, we identified ciliated cells with many

158   small vesicles clustered near multivesicular bodies, mitochondria, and electron-dense structures

159   similar to β-particles of glycogen (**Fig 2E – upper-left and upper-right panels, respectively**).

160   Under higher magnification, we were able to confirm these small vesicles had a double-membrane

161   (**Fig 2E – lower-left panel**) similar to replicative complexes previously described for RV-A and

162   RV-B [30]. Interestingly, some ciliated cells in RV-C15-infected HAE also contained electron-

163   dense structures in their perinuclear region similar to the "viral crystals" observed in cells infected

164   by other picornaviruses (**Fig 2E – lower-right panel**) [32, 33].

165

166   **3. RV-C15 infection triggers fragmentation of Golgi stacks and induces PI4P.**

167   Different cellular membranes can contribute to the formation of replication organelles

168   during viral infection; however, the Golgi is the main source reported for many picornaviruses,

169   including rhinoviruses [31, 34]. Consequently, viral replication is associated with fragmentation of

170   the Golgi stacks and changes in expression of phosphatidylinositol-4-phosphate (PI4P), a Golgi

171   resident lipid [31, 34, 35]. To determine if RV-C replication induced similar effects, we inoculated

172   HAE with RV-C15 – or RV-A16 and RV-A2 as positive controls [35, 36] – and analyzed the Golgi

173   by detection of giantin expression at 12 hpi. While giantin visualization revealed a compact

174   structure close to the nucleus in non-infected HAE (**Fig 3A**), giantin signal was spread throughout

175   the cytoplasm in cells with evidence of active viral replication for all RVs tested (**Fig 3A**). The

176   fragmentation of Golgi structures inferred from our IF data was further supported by TEM, where,

177   compared to the non-infected control, Golgi stacks were barely visible in cells from RV-C15-

178   infected HAE cultures (**Fig 3B**).

179   In addition to a loss of Golgi integrity, we also observed enhanced detection of PI4P in

180   cells with active RV replication compared to non-infected controls. Similar to giantin, PI4P was

181   dispersed throughout the cytoplasm in infected cells (**Fig 3C**). To further assess the changes in

182   giantin and PI4P levels, we compared the CTCF for these cellular targets in both non-infected

183   and infected cells. Our data revealed both giantin and PI4P levels were elevated and strongly

184   correlated in HAE infected with all RVs, though the change in PI4P was not significant for RV-A2

185   (**Fig 3D, 3E and S3 Fig**). A direct relationship was also observed between giantin and dsRNA

186   CTCF in RV-C15- and RV-A16-infected cells while PI4P and viral dsRNA CTCF were only

187   correlated in RV-C15 HAE (**Fig 3E, and S3 Fig**).

188   The close association between Golgi membranes and picornavirus replication has been

189   shown by the colocalization between viral dsRNA and different Golgi markers (e.g., giantin, TGN-

190   46, GM130) [28, 31, 34]. Therefore, we next sought to evaluate the Golgi as a site for RV-C15

191   replication through colocalization analysis of dsRNA with giantin, and PI4P. Despite the strong

192   correlation between giantin and PI4P observed during RV-infection (**Fig 3E and S3 Fig**), the ratio

193   of colocalization between them was very low at pixel-intensity and spatial levels (**S1-3 Tables)**.

194   Surprisingly, the ratios of viral dsRNA/giantin and dsRNA/PI4P colocalization were also low using

195   pixel-intensity based methods (**S4-9 Tables**). The 3D surface plot from RV-C15-infected cells at

196   12 hpi also demonstrated little evidence of colocalization between dsRNA and giantin (**Fig 3F**) or

197   PI4P (**Fig 3G**). Spatial colocalization analysis confirmed these observations, with less than 9% of

198   the total dsRNA detected at the same location as giantin or PI4P in RV-C15-infected cells (**Fig**

199   **3H and 3I, S4-9 Tables**). Thus, despite the fragmentation of the Golgi stacks and increase of

200   PI4P in airway epithelial cells with active RV-C15 replication, our data indicate the Golgi is not the

201   main site for viral genome replication and PI4P is not a marker for sites of RV-C15 replication in

202   HAE as observed for other RVs [31, 34].

203

4. Endoplasmic reticulum is a site for RV-C15 genome replication, but not RV-A16 or RV-A2.

Given the low ratio of colocalization between RV-C15 dsRNA and Golgi markers, we next evaluated ER membranes as a potential site for viral genome replication. WB analysis of the ER-associated protein calnexin in RV-C15-infected HAE did not indicate a significant change compared to non-infected cultures at 12, 24, or 48 hpi (**S4 Fig**). However, at the single-cell level, calnexin fluorescence was not only elevated in cells infected with RV-C15, RV-A16, and RV-A2 compared to the negative control at 12 hpi (**Fig 4A and 4B**) but also directly correlated with fluorescence levels of viral dsRNA (**Fig 4C**). Interestingly, the 3D view of HAE infected with RV-C15 at 12 hpi showed calnexin spread throughout the cytoplasm, and there was a strong indication of calnexin and viral dsRNA colocalization (**Fig 4D**), which was further supported by 3D surface plot data (**Fig 4E**).

Pixel-intensity-based analysis confirmed the high level of colocalization between viral dsRNA and calnexin in cells infected not only with RV-C15 (56.3%), but also RV-A16 (28%) and RV-A2 (49.1%) at 12 hpi (**S10-12 Tables**). However, this high colocalization ratio was only confirmed for RV-C15-infected cells at the 3D level (spatial-colocalization analysis; **Fig 6F and 6G**), suggesting that, unlike RV-A16 and RV-A2, the ER is the main site for RV-C15 genome replication.

5. RV-C15 infection induces incomplete autophagy.

Previous studies have shown picornaviruses, including several rhinoviruses, manipulate the autophagy pathway to mediate non-lytic release of progeny following replication [37]. Since the induction of autophagy is rhinovirus genotype-specific [37-39], we sought to determine if RV-C15 triggered the induction of autophagy in HAE. Towards this goal, we inoculated cultures with RV-C15 alongside RV-A16 and RV-A2 as controls, and probed for Lysosome-associated

229   membrane glycoprotein 1 (Lamp-1; a lysosome marker) and LC3b (an autophagosome marker)

230   by WB. LC3b protein levels were minimal in non-infected HAE, suggesting a low basal rate of

231   autophagy while Lamp-1, LC3b-I, and LC3b-II expression varied across donors and time points

232   during RV-C15 infection. Still, as these proteins were typically elevated at 12 hpi (**Fig 6A**), we

233   further evaluated levels of Lamp-1 and LC3b in HAE by IF at this time point. Lamp-1 and LC3b

234   detection in HAE was significantly stronger in RV-C15- and RV-A2-infected cells while the level

235   of detection in RV-A16-infected HAE was similar to the negative control (**Fig 6B and 6C**).

236   Curiously, the 3D view of non-infected cells revealed an apical localization of Lamp-1 while this

237   protein was spread through the cytoplasm in RV-infected cells (**Fig 6B**). A high correlation ratio

238   between Lamp1 fluorescence levels and dsRNA was obtained in RV-infected cells; however,

239   LC3b levels strongly correlated with dsRNA only in cultures infected with RV-C15 and RV-A2 (**Fig**

240   **6D and S5 Fig**). Together, these data suggest RV-C15 and RV-A2 (but not RV-A16) induce

241   autophagy to significant levels over the baseline in HAE.

242   Since the inhibition of autolysosome formation at the termination of the autophagy

243   pathway is characteristic of picornaviruses that induce autophagy to promote virus release [40],

244   we further evaluated autolysosome formation defined by Lamp-1 and LC3b colocalization. Results

245   from spatial colocalization analysis in cultures infected with RVs indicated greater detection

246   autolysosomes in RV-A16-infected cells compared to RV-C15- and RV-A2-infected cells (**Fig 6E**

247   **and S13-15 Tables**). Thus, these data suggest that, similar to RV-A2 but unlike RV-A16, RV-C15

248   induces incomplete autophagy in HAE.

249

250   **6. STING expression promotes replication of RV-C15 in HAE.**

251   In this study, we observed RV-C15 genome replication in HAE to be associated with the

252   ER (**Fig 4**) and the induction of incomplete autophagy at 12 hpi (**Fig 5**). Interestingly, STING,

253   which localizes to the ER, was recently shown to induce the autophagy pathway during RV-A16

254   infection [41] and was identified as a proviral factor for RV-A and RV-C, but not RV-B, where

10

255 STING overexpression facilitated viral genome replication in Huh-7 cells [24]. Based on these

256 data, we investigated the expression of STING in HAE infected with RV-C15. Interestingly, we

257 found elevated protein levels and the appearance of a second higher molecular weight band at

258 48 hpi compared to non-infected HAE (**Fig 6A**) as well as robust detection by IF in dsRNA(+)

259 ciliated cells at 12 hpi (**Fig 6B**). Notably, 3D view analysis revealed that dsRNA/STING-double

260 positive cells also exhibited dispersed distribution of acetylated alpha-tubulin, suggesting STING

261 levels increase as replication progresses (**Fig 6C**). Indeed, the CTCF of STING not only increased

262 significantly in HAE infected with RV-C15 (**Fig 6D**), but also strongly correlated with dsRNA levels

263 at 12 hpi (**Fig 6E**). However, despite the 3D surface plot and pixel-intensity colocalization analysis

264 suggesting high level of dsRNA/STING colocalization in RV-C15-infected HAE (**Fig 6F and S16**

265 **Table**), spatial colocalization analysis indicated the median colocalization ratio between both

266 targets was lower than 5% (**Fig 6G**).

267 To better understand the importance of STING to RV-C15 genome replication, we

268 genetically knocked-out STING using a CRISPR/Cas9 approach in immortalized human airway

269 epithelial cells (BCi-NS1.1 cells [42]), differentiated them into HAE cultures (**Fig 6H**), and infected

270 them with RV-C15, RV-A16, or RV-B14. Immunofluorescence detection of dsRNA at 12 hpi

271 confirmed the susceptibility of control cultures expressing a non-targeting guide RNA to RV-C15,

272 RV-A16, and RV-B14 infection (**Fig 6I**). However, the frequency of dsRNA (+) cells was lower in

273 STING-depleted HAE infected with RV-C15 and RV-A16 (**Fig 6I**). While infection with RV-B14

274 was less efficient overall, a similar frequency of dsRNA+ cells were observed in both control and

275 knockout HAE (**Fig 6I**). STING-knockout cultures also had significantly lower intracellular viral

276 RNA copy numbers for RV-C15 and RV-A16 but not RV-B14, further validating our results (**Fig**

277 **6J**) and suggesting that the increase of STING expression in RV-C15-infected HAE has an

278 advantageous impact on viral genome replication.

279

7. RV-C15 infection alters epithelial permeability, disposition of tight junction-associated proteins, and mucociliary clearance.

Our results to this point highlight RV-C15-induced cytopathic effects at the single-cell level in HAE (**Fig 1-5**). To extend these observations, we quantified extracellular lactate dehydrogenase (LDH) at the culture-level as an indication of plasma membrane leakage. LDH release was restricted to the apical compartment and did not exceed 20% of the maximum levels obtained from lysed control cultures; however, LDH levels increased over time (**Fig 7A**) in line with RV-C15 replication kinetics (**Fig 1A and 1B**). Thus, we sought to further evaluate the global impact of RV-C15 infection on epithelial integrity. Interrogation of HAE permeability during RV-C15 infection revealed a significant, albeit transient, decrease in transepithelial electrical resistance (TEER) at 12 hpi (**Fig 7B**). Since the transepithelial transport of ions is mediated by pores formed by integral membrane proteins termed claudins [43], we next investigated the expression and localization of claudin-1 during RV-C15 infection in HAE. While claudin-1 protein levels in cultures infected with RV-C15 did not vary (**Fig 7C**), we observed a change in claudin-1 distribution in RV-C15-infected cells at 12 hpi by IF (**Fig 7D**). To determine if this translocation was specific to claudin-1, we characterized Zona occludens 1 (ZO-1), a cytoplasmic tight junction-associated protein. Similar to claudin-1, ZO-1 protein levels for both subunits (ZO-1 +α and ZO-1 -α) did not vary in RV-C15-infected HAE compared to the negative control (**Fig 7C**), while ZO-1 disposition was more widespread in dsRNA(+) cells (**Fig 7E**). To quantify the effect of RV-C15 infection on ZO-1 disposition over time, we utilized the Junction Analyzer Program (JAnaP) [44-46], which allowed us to assess the profile of ZO-1 detected in non-infected and RV-C15-infected cells (**Fig 7F**). The increase of discontinuous ZO-1 quantified in this assay (**Fig 7G**) indicates the ZO-1 translocation in HAE (**Fig 7E**) parallels the progression of RV-C15-infection. Additionally, two profiles of discontinuous ZO-1 were evaluated, and ZO-1 was found in a more perpendicular than punctual disposition in RV-C15- infected HAE (**Fig 7H and 7I**).

12

305   Given the ciliated cell tropism RV-C15 and the important role of these cells in promoting

306   mucociliary clearance (MCC), we also assessed the global impact of RV-C15 infection on mucus

307   transport. HAE cultures were equilibrated at 34°C and the transport rate of red-fluorescent

308   microspheres in the extracellular mucus gel was calculated immediately prior to inoculation, and

309   up to 48 hpi. IF confirmed viral replication at 12 hpi in HAE inoculated with viable, but not UV-

310   inactivated, RV-C15 (**S6 Fig**). The transport of microspheres indicated a slight increase in MCC

311   in HAE inoculated with PBS and a similar, albeit significant, elevation in microsphere transport

312   rate in UV-inactivated RV-C15-inoculated cultures at 12 hpi (**Fig 7J**), likely attributable to the

313   addition of fluid on the apical surface after the T=0 time point. Despite this, RV-C15 infection

314   resulted in a significant decrease in MCC at both 12 and 24 hpi (**Fig 7J**) indicating viral replication

315   impairs this innate host defense mechanism.

316

Discussion

318   Rhinovirus is becoming increasingly recognized as a cause of both upper and lower

319   respiratory tract infection [4-8]. Furthermore, the risk for development of asthma in children after

320   infection by RV, especially RV-C [8, 13, 14], highlights the clinical relevance of these viruses. Due

321   to restricted receptor expression in traditional immortalized cell culture systems [26], we

322   investigated RV-C15 replication using an *in vitro* model of HAE that supports the entire RV-C life

323   cycle. Previous studies in similar systems have shown the impact of temperature and cell

324   differentiation stage on RV-C replication [22, 25, 27]. Here, we detail a multi-step replication curve

325   for RV-C15 (**Fig 1A and 1B)**, indicating the peak of intracellular viral load at 12 hpi by qPCR and

326   IF (**Fig 1A and 1B, S1A Fig**) and peak viral release at 24 hpi (**Fig 1A and 1B**) in agreement with

327   a previous report characterizing RV-C11 and RV-C15 infection in bronchial cells [26].

328   In well-differentiated HAE, we detected CDHR3 on the apical surface of ciliated cells (**Fig**

329   **1C-1E**). Interestingly, we did not observe any evidence of cytosolic CDHR3 in non-infected cells,

330   differing from previous immunofluorescence data [21, 23] but in agreement with CDHR3 detection

331   on cilia by TEM [21]. However, CDHR3 distribution changed, and fluorescence levels decreased,

332   in RV-C15-infected cells (**Fig 1C-1E, and 1G**) without altering levels of acetylated alpha-tubulin

333   or FoxJ1 (**S1G and S1H Fig**). Unlike ICAM-1 and LDLR (receptors for RV-A and RV-B,

334   respectively), the dynamics of CDHR3 during infection and associated pathway(s) of RV-C entry

335   remain unknown. After endocytosis of RV-A and RV-B particles, ICAM-1 and LDLR are either

336   degraded in the lysosome with empty capsids, or LDLR is trafficked from the endosome to be

337   recycled [47]. The intracellular distribution of CDHR3 after RV-C15 infection in HAE suggests

338   CDHR3 follows the same path as other RV receptors. In contrast, global expression of CDHR3

339   protein quantified by WB increased 4-fold at 12 hpi in RV-C15 infected epithelium (**S1F Fig)**.

340   Since the function of CDHR3 is unknown, the trigger for this elevated expression and what impact

341   this may have on infection remains unclear. Nonetheless, similar up-regulation was detected for

342   ICAM-1 and LDLR in primary cell cultures and human volunteers after RV infection [48-50].

343   After confirming the susceptibility of our HAE models to RV-C15 infection, we further

344   investigated the localization and association of replication complexes with various organelle

345   markers at the single-cell level. Using dsRNA as a marker for virus replication, we observed both

346   perinuclear and "ring-like" distribution of replication centers closer to the basolateral membrane

347   during RV-C15, RV-A16, and RV-A2 replication (**Fig 2A-2C and S2A-S2D Fig)**. To our knowledge,

348   the latter profile has not been described during RV or any other picornavirus infection, and our

349   TEM data indicates the formation of large intracellular vesicles filled with unknown electron-dense

350   content may be the underlying cause of altered dsRNA disposition. Whether these large vesicles

351   play a specific role in RV replication or if they are simply indicative of cellular changes that precede

352   cell death is unknown.

353   Notably, our TEM analysis also identified smaller, double-membraned vesicles, similar to

354   those identified during replication of other RVs and related picornaviruses [28-31], that likely

355   represent sites of RV-C15 genome replication (**Fig 2D and 2E**). Prior reports identified the

14

356   induction of replicative complexes derived from the ER by the poliovirus 2BC and 3A proteins [51,

357   52] and these same proteins in RV-A16 were associated with the ER at an early stage of viral

358   infection [35]. Nonetheless, work to date suggests the Golgi is the primary site for picornavirus

359   genome replication [28, 31, 34]. Further, the formation of replicative complexes has been

360   associated with cholesterol exchange driven by OSBP1 [31], accumulation of ER-vesicles

361   resulting from the inhibition of ERGIC-to-Golgi transport [36], and fragmentation of Golgi stacks

362   induced by the viral 3A protein [34, 35]. In this study, we observed an increase of giantin and PI4P

363   levels, dissolution of Golgi stacks, and spread of PI4P-positive vesicles in RV-C15-infected cells

364   (**Fig 3A-D)** suggesting RV-C impacts Golgi membranes similar to other picornaviruses. However,

365   despite the strong correlation between dsRNA and fluorescence levels of both giantin and PI4P

366   (**Fig 3E**), colocalization analysis indicated neither giantin- nor PI4P-positive vesicles are the main

367   site for RV-C15 genome replication (**Fig 3H and-3I**). Similar observations were made in RV-A16-

368   infected HAE (**Fig 3**) although dsRNA fluorescence levels only strongly correlated with giantin

369   and not PI4P (**S3A Fig**). These data were unexpected, as prior work in HeLa and nasal epithelial

370   cells noted PI4P enrichment of Golgi membranes during RV-A16 genome replication [31].

371   Different from the literature [31], Golgi and PI4P-positive vesicles were not the main site for RV-

372   A2 genome replication in HAE either (**Fig 3H and 3I**), and neither the significant increase in levels

373   of giantin nor insignificant increase in PI4P correlated strongly with viral dsRNA (**Fig 3D and S3B**

374   **Fig**).

375   Most notably, our results identified the ER as the main site for RV-C15 replication through

376   elevated levels of calnexin in RV-infected HAE (**Fig 4A and 4B**) and a high ratio of

377   dsRNA/calnexin colocalization in cells infected with RV-C15, but not RV-A2 and RV-A16 (**Fig 4E-**

378   **G**). The increase in calnexin levels observed in this study could be the result of ER stress in

379   infected cells, as reported for RV-A1B and RV-A16 [53, 54]. The RV-A16 2B protein [54] forms

380   pores on ER membranes, promoting calcium ion efflux, which increases membrane permeability

381   and triggers stress. These effects on ER membranes have been associated with more efficient

15

382 release of vesicles that may represent additional sites for picornavirus replication [55]. Notably,

383 inhibition of ER stress resulted in a decrease in RV-A1B replication [53], corroborating the

384 hypothesis that ER-derived vesicles are a site for viral replication [55] and supporting our

385 conclusion that RV-C15 replication is associated with the ER in HAE (**Fig 4E-G**).

386 In the final stages of the viral life cycle, progeny picornavirus virions are released through

387 cell lysis or by usurping the autophagy pathway [37-39]. Exploitation of the autophagy pathway

388 was originally shown for poliovirus [40] and is characterized by virus-mediated inhibition of

389 autolysosome formation and release of autophagosomes full of nascent virions that likely protect

390 particles from the immune response [38]. As expected [39], RV-A2 induced autophagy in HAE in

391 contrast to RV-A16 (**Fig 5B and 5C**) based on elevated Lamp1 and LC3b levels. However, a very

392 low ratio of Lamp-1/Lc3B colocalization indicated a failure to form autolysosomes (**Fig 5E**). The

393 results obtained in RV-C15-infected HAE were similar to RV-A2, indicating the induction and

394 manipulation of the autophagy pathway **(Fig 5B, 5C, and 5E)**. To our knowledge, this is the first

395 time the autophagy pathway has been analyzed during RV-C infection.

396 The identification of ER as a site for genome replication and induction of autophagy during

397 RV-C15 infection of HAE led us to investigate STING, a protein that has been associated with

398 induction of ER stress and autophagy [41, 56]. In this study, we detected an increase in STING

399 expression in RV-C15-infected HAE (**Fig 6A, 6B, and 6D**) which correlated with levels of dsRNA

400 (**Fig 6E**). However, this correlation was not related to a close interaction between STING and

401 dsRNA, as the median colocalization ratio at the spatial level was lower than 5% (**Fig 6G**).

402 Additionally, the absence of STING impacted viral genome replication, resulting in significantly

403 lower intracellular viral RNA levels at 12 hpi for RV-C15 and RV-A16, but not RV-B14 (**Fig 6I and**

404 **6J**). These data, which assayed endogenous STING expression in RV-infected HAE, corroborate

405 published data in undifferentiated cells indicating STING expression is important for RV-A and

406 RV-C genome viral replication [24]. STING is a ER-resident transmembrane protein which can be

407 phosphorylated by TANK-binding Kinase I (TBK1) or translocated to the ER-Golgi intermediate

408   compartment (ERGIC) before phosphorylation [57]. The phosphorylation of STING in the ER is

409   necessary for autophagy induction during RV-A16 infection [41], while the translocation to the

410   ERGIC is required for ER stress [56]. The low ratio of dsRNA/STING spatial colocalization at 12

411   hpi (**Fig 6G**) is surprising and indicates that either genome replication of RV-C15 occurs at

412   different sites on ER membranes (STING-negative) or most of STING had already been

413   translocated to ERGIC. RV-C15 replication also induced autophagy in HAE, though more

414   experiments are needed to relate this phenomenon to STING activation.

415   Given the observed impacts of RV-C15 replication in infected cells, we further probed the

416   effects of viral infection on epithelial integrity and functionality. The level of cytotoxicity of RV-C15

417   infection in HAE, measured by LDH release, increased overtime in the apical compartment only

418   (**Fig 7A**), in agreement with viral cellular tropism for ciliated epithelial cells that face the luminal

419   surface of the airway **(Fig 1)** [22, 25]. The dissociation of tight junctions during viral infection,

420   including RV-A and RV-B, has been associated with loss of epithelial-selective permeability and

421   increase in bacteria translocation across the epithelium [58]. A previous analysis of RV-A16, RV-

422   A1B, and RV-A39 found the reduction of TEER and increase in epithelium permeability for inulin

423   were associated with both claudin-1 and ZO-1 dissociation [58]. Similar to these reports, RV-C15

424   temporarily increased epithelial permeability to small particles and ions (as indicated by a

425   temporary loss in TEER, **Fig 7B**) which may be due, at least in part, to claudin-1 translocation

426   (**Fig 7C and 7D**). Additional claudins (e.g., claudin-3, -4 and -5) that are also expressed in the

427   airway epithelium and known to impact transcellular transport were not assayed here [59, 60].

428   Still, the altered expression of tight junction proteins was not restricted to claudin-1 as we also

429   detected ZO-1 throughout the cytoplasm in dsRNA(+) cells without any change in overall protein

430   levels during infection (**Fig 7C and 7E**). Despite being a tight junction protein, ZO-1 interactions

431   are more important to cell polarization and paracellular permeability [61]. Although we did not

432   check paracellular transport of large particles, disrupted states for ZO-1 that indicated progressive

433   translocation with ongoing viral infection (**Fig 7F-I**) could impact cellular organization.

17

434 Nonetheless, the loss of TEER and changes in claudin-1 and ZO-1 observed in this study for RV-

435 C15 were less dramatic than previous reports for RV-A and RV-B [37, 39, 58].

436   Beyond epithelial barrier integrity, we also found RV-C15 infection impacts mucociliary

437 clearance functionality. Similar to a previous study [62], MCC decreased significantly after 12 hpi

438 in HAE infected with RV-C15 but not UV-inactivated virus, indicating that active viral replication

439 interferes with this cellular mechanism of pathogen removal (**Fig 7J**). We speculate that the

440 temporary increase in MCC observed in cultures inoculated with UV-inactivated virus is due to

441 the addition of fluid on the apical surface. However, this increase was not significant for the

442 negative control and therefore may indicate that the host response to incoming viral particles

443 stimulates MCC. The coordinated beating of ciliated cells drives the basal MCC rate of ~5.5

444 mm/min, which can be altered by mucus composition, temperature, and humidity [63-65]. Indeed,

445 mucus hypersecretion [66] and changes in mucus composition [67] are both associated with RV

446 infections. In this study, we noted altered distribution of acetylated alpha-tubulin in cells with active

447 viral replication (**Fig 1D and 1F**) which likely indicates impaired cilium structure and function in

448 these cells. Whether the progressive loss of cilia function and eventual death of infected cells

449 contributes to our observed change in MCC during RV-C15 infection is not clear.

450   In conclusion, our present study expands our current understanding of RV replication in a

451 physiologically-relevant setting, substantiating previous observations related to virus-induced

452 membrane reorganization, and demonstrating that RV-C15 displays many typical features of

453 picornavirus infection. In addition, we identify RV-C15 replication in association with ER

454 membranes unlike previously characterized RVs. While we speculate that these data identify a

455 unique feature of RV-C replication, our study is limited by the use of only one RV-C genotype;

456 thus, further analysis to confirm these observations using additional RV-C isolates is important.

457 Notwithstanding, our findings underscore the fact that virus-host interactions critical for rhinovirus

458 replication are not always conserved, possibly contributing to their different clinical profiles, and

459 supporting further investigation into this group of pathogens.

460

Materials and Methods

1. Primary and immortalized cell culture and viral stocks.

Human airway tracheobronchial epithelial cells isolated from airway specimens from donors without underlying lung disease were provided by Lonza, Inc. Primary cells derived from single patient sources were expanded on plastic and subsequently plated (5×10^4 cells / well) on rat-tail collagen type 1-coated permeable transwell membrane supports (6.5 mm, #3470; Corning, Inc., Corning, NY). HAE cultures were grown in Pneumacult-Ex basal medium (#05008, StemCell Technologies, Seattle, WA), or Pneumacult-ALI medium (#05001, StemCell Technologies, Seattle, WA) with provision of an air-liquid interface for approximately 6 weeks to form differentiated, polarized cultures that resemble *in vivo* pseudostratified mucociliary epithelium.

H1 HeLa (#CRL-1988; ATCC, Manassas, VA) and HEK-293T (#CRL-11268; ATCC) cells were cultivated in Dulbecco's Modified Eagle Medium (DMEM; #11965118; Gibco – Thermo Scientific, Waltham, MA) supplemented with fetal bovine serum (FBS; GenClone FBS; Genesee Scientific, San Diego, CA) and 1% penicillin/streptomycin (#15140122; Gibco). All cell cultures were maintained at 37°C with 5% CO_2.

RV-C15, RV-A2, RV-B14, and RV-A16 were rescued from infectious clones kindly donated by Drs. James Gern and Yuri A. Bochkov, (pRV-C15), Dr. Wai-Ming Lee (pRV-A2) and Dr. Ann Palmenberg (pRV-B14 and pRV-A16) from University of Wisconsin – Madison. Rescue of infectious RV was done according to published protocols [68, 69] in H1 HeLa cells, with one modification: viral RNA transfection was performed using jetPRIME reagent (#114-07; Polyplus transfection, Illkirch, France).

482

2. CRISPR-Cas9-mediated knockout of STING in HAE.

484   Single guide RNAs (sgRNA) targeting STING or no known target (NTC) and flanked by

485   restriction sites for cloning into the pLentiCRISPRv2 backbone [69] with eGFP replacing

486   puromycin selection were as follows: sgRNA1- 5'-CACCGCATATTACATCGGATATCTG-3' and

487   5'-AAACCAGATATCCGATGTAATATGC-3';   sgRNA2-   5'-

488   CACCGACTCTTCTGCCGGACACTTG-3'   and   5'-AAACCAAGTGTCCGGCAGAAGAGTC-3';

489   NTC-   5'-CACCGGCACTACCAGAGCTAACTCA-3'   and   5'-

490   AAACTGAGTTAGCTCTGGTAGTGCC-3'. Lentiviral stocks were generated by co-transfection of

491   1µg pLentiCRISPRv2 (Addgene plasmid #52961 donated by Dr. Feng Zhang) [70], 0.2 µg pCMV-

492   VSV G (Addgene plasmid #8454 donated by Dr. Bob Weinberg) [71]), and 0.7 µg psPAX2

493   (Addgene plasmid #12260 donated by Dr. Didier Trono) into HEK-293T cells with jetPRIME

494   reagent (Polyplus transfection). Lentivirus-laden supernatant was collected and replaced at 24

495   hour intervals up to 72 hours, pooled, and filtered to remove viable cells and debris.

496   For target cell transduction, lentivirus-containing supernatants were applied to BCi-NS1.1

497   cells (kindly provided by Drs. Matthew Walters and Ronald Crystal [42]), maintained as HAE at

498   40-60% confluence with a final concentration of 20 mM HEPES (Gibco) and 4 µg/mL polybrene

499   (Thermo Scientific). Cells were then centrifuged (1,000 x g for one hour at 37°C) and incubated

500   at 37°C with 5% CO_2 for 6 hr. The inoculum was removed and replaced with fresh Pneumacult-

501   Ex Plus media (StemCell Technologies). At 60-80% confluence, eGFP-positive cells were

502   enriched by fluorescence-activated cell sorting on a BD FACSAria-II Cell Sorter (BD Bioscience,

503   San Jose, CA). These sorted BCi-NS1.1 cells were then expanded, seeded at 3.3×10^4 cells/well

504   on 6.5mm rat-tail collagen type I-coated transwell membranes, and cultured at air-liquid interface

505   as previously described for HAE.

506

507   3. Titration of rhinoviruses by plaque assay and quantitative real-time PCR (qPCR).

508   RV-A2, RV-B14, and RV-A16 stocks were titrated by plaque assay method using H1 HeLa

509   cells plated in 24-well dishes and a published protocol with modifications [72]. Briefly, 90%

510   confluent H1 HeLa monolayers were inoculated with ten-fold serial dilutions of the viral stock in

511   McCoy's medium with 2% FBS and 30mM $MgCl_2$. After 1 hour incubation at room temperature

512   (RT), the inoculum was exchanged for a semi-solid overlay composed of 0.6% of bacteriological

513   agar (#A5306; Sigma-Aldrich, Saint Louis, MO) in DMEM-F12 (#12500062; Gibco),

514   supplemented with 1% FBS (Genesee), 1% penicillin/streptomycin (Gibco), 1% L-glutamine

515   (#25030081; Gibco), and 30mM $MgCl_2$ (Sigma-Aldrich). The plate was incubated at 34°C for 72

516   hours and the cells were fixed with 38% formaldehyde (#47608; Sigma-Aldrich) in a 0.15M saline

517   solution. The fixing solution was removed together with the overlay after a 24-hour incubation at

518   RT and plaques visualized by staining the monolayer with 0.1% crystal violet (#C0775; Sigma-

519   Aldrich) diluted in a 20% ethanol (200 proof) solution.

520   RV-C15 was titrated by qPCR, which was also used to quantify RV-A16 and RV-B14 in

521   experiments done in CRISPR/Cas9-modified HAE. To quantify viable viral particles, 10µl of RV-

522   C15 stock or 100µL of experimental sample was first treated with 1u RNase A (#EN053; Thermo)

523   and 1u DNase I (#18047019; Invitrogen – Thermo Scientific) for 1 hr at 37°C. Viral RNA was then

524   extracted using a QIAamp Viral RNA Mini Kit (#52904; Qiagen, Hilden, Germany); total RNA was

525   extracted from cells using a RNeasy Mini Kit (#74104; Qiagen). Next, up to 1µg of RNA was used

526   in a reverse transcription reaction (High Capacity cDNA Reverse Transcriptase Kit; #4368814;

527   Applied Biosystem – Thermo), with random hexamer primers, as per the manufacturer's protocol.

528   qPCR was done using 3µl of cDNA, 10pM of HRVTF63 forward (5'–

529   ACMGTGTYCTAGCCTGCGTGGC–3') and HRVTR reverse (5'–GAAACACGGACACCCAAAGT

530   GT–3') primers, 10pM HRVTF probe (5'–FAM/TCCTCCGGCCCCTGAAT/BHQ1–3'), and

531   LuminoCT Taqman Master Mix (#L6669; Sigma-Aldrich) according to the manufacturer's protocol.

532   For absolute quantification, a standard curve was delineated using cDNA generated from ten-fold

533   serial dilutions of *in vitro*-transcribed pRV-C15, pRV-A16, and pRV-B14.

534

535   **4. RV-infection in HAE and H1 HeLa cells.**

536   One week before the experiment in HAE, cells were washed 3 x 30 minutes with 100µl of

537   phosphate buffered saline (PBS; #P5119; Gibco) at 37°C to remove excessive mucus. In

538   CRISPR/Cas9-modified BCi-NS1.1-derived HAE an additional wash was performed immediately

539   before inoculation. HAE cultures were inoculated on the apical surface with 10µl of PBS (negative

540   control), sucrose-purified RV-C15 (10^{10} copies of RNA), RV-A16 ($5x10^5$ PFU), RV-B14 ($5x10^5$

541   PFU), or RV-A2 ($5x10^5$ PFU) and incubated at 34°C with 5% CO_2 until sample collection. In the

542   replication curve and cytotoxicity assays, the inoculum was removed, and the apical surface

543   rinsed with PBS, at 4 hpi.

544   For HAE culture sample collection, 100µl of PBS (Gibco) was added to the apical chamber

545   and harvested after a 30-minute incubation at 34°C; basolateral samples (500µl ALI media) were

546   collected directly from underneath the culture. Cells were harvested from the transwell

547   membranes using 350µl RLT buffer (#74104; Qiagen) for downstream RNA extraction, or 75µl of

548   Radio Immuno-Precipitation Assay (RIPA) buffer (#89900S; Thermo) plus protease inhibitors

549   (#88666; Thermo Scientific) for subsequent Western blot (WB) assays. The aliquots for RNA

550   extraction and WB were stored at -80ºC and -20ºC, respectively. Alternatively, cultures were fixed

551   with 4% (w/v) freshly-prepared paraformaldehyde (#157-8-100; Electron Microscopy Sciences

552   (EMS), Hatfield, PA) for immunofluorescence (IF) assays or 2% (w/v) glutaraldehyde in 0.1M

553   cacodylate buffer for downstream transmission electron microscopy analysis.

554

555   **5. IF assays in HAE and H1 HeLa cells.**

556   HAE cultures were fixed with 100µl (apical) and 500µl (basolateral) 4% (w/v) freshly

557   prepared paraformaldehyde (#157-8-100; EMS). After a 15-minute incubation at RT, the culture

558   was washed once for 3 minutes with PBS and then incubated for 10 minutes at RT with a

559   quenching solution (25mM NH_4Cl diluted in PBS) before being washed twice for 3 minutes each

560   with PBS. Permeabilization of cell membranes was done using 0.2% Triton-X diluted in PBS; after

561   a 15-minute incubation at RT, the cells were washed 3 x 3 minutes with PBS. A blocking solution

562 (10% normal donkey (#017-000-121) or normal goat serum (#005-000-121, Jackson

563 ImmunoResearch Labs, West Grove, PA) diluted in PBS with 0.2% Tween-20) was added and

564 only removed from the apical side after a 10-minute incubation at RT. The apical surface of the

565 culture was washed 3 x 3 minutes with PBS. Primary antibody diluted in PBS with 0.2% Tween-

566 20 and 1% Bovine Serum Albumin (BSA; #BP9700100; Fisher Scientific, Hampton, NH) was

567 added to the apical chamber and incubated overnight at 4°C, protected from light. The apical

568 surface was washed 3 x 5 minutes with PBS and incubated with the secondary antibody diluted

569 in PBS with 1% BSA. After a 2-hour incubation at RT, protected from light, the secondary antibody

570 solution was removed and the apical surface of HAE was washed 3 x 5 minutes with PBS. If

571 necessary, additional stains were done by repeating this protocol; reducing the secondary

572 antibody incubation to 20 minutes when the next primary antibody applied was generated in the

573 same species as another primary antibody used in the same experiment. Fluorescent-conjugated

574 primary antibodies were applied during the final round of staining, where applicable. Nuclei were

575 visualized in the final step by adding 1ng/ml of Hoechst 33342 (#H3570; Invitrogen, Thermo)

576 diluted in PBS with 0.2% Tween-20 to the apical surface. After a 5-minute incubation at RT, the

577 cultures were washed 3 x 5 minutes with PBS, after which the transwell membrane was separated

578 from the plastic holder and mounted on a glass slide using VectaShield Antifade mounting

579 medium (#H-1000-10; Vector Laboratories, Burlingame, CA) and 1.5mm-thick cover glass.

580   Images were acquired with a Zeiss Axio Observer 3 Inverted fluorescence microscope

581 (Cell Observer HS image system, Zeiss Axiocam 503 mono camera, optimal acquisition mode,

582 AIM-Zen 2007 software) equipped with EC-Plan-NEOFLUOR 20x/0.5NA Ph2 and 40x/0.75NA

583 Ph2 air objectives. Higher resolution images and z-series optical sections (at 1μM intervals) were

584 acquired with a LSM710 Zeiss confocal microscope (Argon laser, pinhole of 1 airy unit (AU), zoom

585 factor of two, optimal acquisition mode, AIM-Zen 2009 software) equipped with a 63x/1.4NA Oil

586 DIC Plan Apo objective at the Imaging Core, University of Maryland, College Park. All images

587 were analyzed using Fiji – ImageJ v.2.1.0/1.53c software [73]. Z-series from a pre-selected region

23

588   of interest (ROI) are displayed as maximum intensity z-projection, orthogonal views (XY, XZ and

589   YZ planes), and 3D surface plots; they were also used for 3D volume reconstruction (3D view)

590   using Fiji [73].

591   The IF protocol described above was used in all assays with the following exception: for

592   PI4P detection, permeabilization was done using a 20mM Digitonin solution (diluted in PBS).

593   Antibodies used in this study are listed in the tables below.

594

595   **Table 1: Primary antibodies used in Immunofluorescence assays.**

Primary Antibody	Dilution	Catalog #	Source
Mouse IgG2a anti-dsRNA (J2) mAb	1:1000	#10010200	SCICONS, Budapest, Hungary
Mouse IgG2b anti-acetylated alpha-tubulin (6-11B-1) mAb A647- conjugated	1:50	#sc-23950-AF647	Santa Cruz Biotechnology Incorporation, Dallas, Texas
Mouse IgG1 anti-FoxJ1 mAb (2A5)	1:200	#14-9965-82	Invitrogen – Thermo
Rabbit IgG anti-claudin-1 mAb [EPRR18871]	1:500	#ab211737	Abcam, Cambridge, UK
Goat IgG anti-calnexin polyclonal antibody	1:500	#PA5-19169	Thermo
Rabbit IgG anti-giantin pAb - Golgi Marker	1:500	#ab80864	Abcam
Rabbit IgG anti-cadherin-28 (CDHR3) pAb	1:500	#orb182906	Biorbyt, Cambridge, UK
Rabbit IgG anti-Lamp1 (D3D11) mAb	1:500	#9091	Cell Signaling, Danvers, MA
Rabbit IgG anti-LC3b (EPR18709) mAb A647-conjugated	1:100	#ab225383	Abcam
Mouse IgM anti-PI(4)P (clone PI4-2) mAb	1:200	#Z-P004	Echelon Bioscience, Salt Lake City, Utah
Rabbit IgG anti-TM173/STING polyclonal antibody	1:100	#19851-1AP	Proteintech, Rosemont, IL

596

597   **Table 2: Secondary antibodies used in Immunofluorescence assays.**

Secondary Antibody	Dilution	Catalog #	Source
Donkey anti-mouse IgG H&L 2°Ab A594-conjugated	1:500	#ab150108	Abcam
Donkey anti-goat IgG H&L 2°Ab A488-conjugated	1:500	#a150129	Abcam
Donkey anti-rabbit IgG H&L 2°Ab A647-conjugated	1:500	#ab150075	Abcam

24

Donkey anti-rabbit IgG H&L 2°Ab A555-conjugated	1:500	#ab150074	Abcam
Goat anti-mouse IgG2a 2°Ab A555-conjugated	1:200	#A21137	Thermo
Goat anti-mouse IgG1 2°Ab A488-conjugated	1:200	#A21121	Thermo
Goat anti-mouse IgM (heavy chain) 2°Ab A647-conjugated	1:200	#A21238	Thermo

598

6. Quantification of fluorescence levels and colocalization analysis.

599

600   The .CZI files from z-stacks collected with a step-size at 1μM were analyzed at region and

601   single-cell levels using Fiji - ImageJ v.2.1.0/1.53c software [73]. For single-cell analysis, the

602   selection of the region of interest (ROI) was based on positivity for dsRNA(+) in RV-infected HAE.

603   At least 5 cells per region were selected to increase rigor.

604   Quantification of fluorescence levels was done in ROI single-cell images following the

605   Corrected Total Cell Fluorescence (CTCF) method [74]. Total CTCF (equal to the sum of CTCF

606   per slice / sample) was calculated per channel and statistically significant differences determined

607   by Mann-Whitney U (Two-tailed; $p<0.05$ significance; 0.95% confidence interval) using Prism

608   GraphPad v.9 software (GraphPad Software, San Diego, CA). Individual CTCF values were used

609   in correlation analysis by the Spearman method (Two-tailed; $p<0.05$ significance; 0.95%

610   confidence interval) using Prism GraphPad v.9 (GraphPad Software).

611   To evaluate the ratio of colocalization between two markers, the background was subtracted

612   from ROI single-cell images following application of a threshold model and watershed filter to

613   better identify the centroids. The final images were first used in colocalization analysis by pixel-

614   intensity based methods (Pearson, threshold Manders, and Van Steensel's methods), followed

615   by spatial analysis based on the distance between centers of mass [75]. All colocalization analysis

616   was done using the Just Another Co-localization Plug-in (JACoP) plugin from Fiji [75].

617

7. Transmission Electron Microscopy (TEM) in HAE.

618

619   The TEM protocol used in this study was based on published methods [29] with

620   modifications, as follows: Cultures were fixed with 2% (w/v) glutaraldehyde in 0.1M cacodylate

621   buffer (100μl on top and 500μl on the bottom) for 60 minutes at RT. The transwell membranes

622   were then separated from the plastic holder and transferred to a new 24-well plate where a second

623   fixation step was carried out with 1% of osmium tetroxide (OsO_4) in 0.1M cacodylate buffer plus

624   1% potassium ferricyanide ($K_3Fe(CN)_6$). Two percent uranyl acetate (diluted in distilled H_2O) was

625   used as post-fixative. The membrane was then incubated in propylene oxide before being

626   embedded in Spurr's Resin. The samples were sectioned to 60–90 nm with a diamond knife

627   (DiATOME) and ultramicrotome (Reichart-Jung) and two slices were placed per copper grid

628   (EMS). The images were obtained using a Hitachi S-4700 Field Emission Scanning Electron

629   Microscope with transmitted electron detector in the Laboratory for Biological Ultrastructure,

630   University of Maryland, College Park.

631

632   **8. Immunoblotting assays.**

633   Total protein in cell lysates (stored at -20ºC in RIPA buffer) were quantified by BCA Protein

634   Assay (#23225; Pierce). A total of 20μg per sample (or 25μg and 30μg for STING and ZO-1 blots,

635   respectively) was then separated on Novex WedgeWell 4-20% Tris-Glycine gels (#XP04202BOX;

636   Invitrogen-Thermo) and transferred to PVDF membranes. Membranes were blocked with 5% non-

637   fat milk solution (diluted in 0.1% Tween-20 in Tris-buffered saline (TBS-T)) or 3% BSA (diluted in

638   TBS-T) for the detection of the tight junction proteins and incubated overnight at 4ºC with the

639   primary antibody. Following a series of washes in TBS-T, membranes were incubated for 1 hr at

640   RT with the appropriate peroxidase-conjugated secondary antibody. All antibodies were diluted

641   in 5% non-fat milk TBS-T solution. Blots were visualized using SuperSignal West Femto Maximum

642   Sensitivity Substrate (#34094; Thermo) or SuperSignal West Dura Extended Duration Substrate

643   (#34075; Thermo).

644

645 **Table 3: Primary and secondary antibodies used in immunoblotting assays.**

Primary Antibody	Dilution	Catalog #	Source
Mouse IgG2b anti-acetylated alpha-tubulin (acetyl K40) monoclonal antibody	1:5000	#ab24610	Abcam
Mouse IgG1 anti-FoxJ1 monoclonal antibody (2A5)	1:1000	#14-9965-82	Invitrogen – Thermo
Rabbit IgG anti-CDHR3 polyclonal antibody	1:1000	#HPA011218	Atlas - Sigma-Aldrich
Goat IgG anti-calnexin polyclonal antibody	1:1000	#PA5-19169	Thermo
Rabbit IgG anti-Lamp1 (D3D11) monoclonal antibody	1:1000	#9091	Cell Signaling
Mouse IgG2b anti-LC3b monoclonal antibody	1:1000	#83506	Cell Signaling
Goat IgG anti-calnexin polyclonal antibody	1:1000	#PA5-19169	Thermo
Mouse IgG2b anti-claudin-1 monoclonal antibody	1:1000	#sc-166338	Santa Cruz
Rabbit IgG anti-ZO-1 polyclonal antibody	1:200	#61-7300	Invitrogen
Mouse anti-β-Actin (clone AC-15) monoclonal antibody, peroxidase-conjugated	1:15000	#A3854	Sigma-Aldrich
Rabbit IgG anti-TM173/STING monoclonal antibody	1:1000	#66680-1-Ig	Proteintech
Secondary Antibody	**Dilution**	**Catalog #**	**Source**
Recombinant mouse IgGk light chain binding protein conjugated to Horseradish Peroxidase (HRP)	1:10000	#sc516102	Santa Cruz
Donkey anti-Goat IgG HRP- conjugated	1:10000	#A15999	Thermo
Goat anti-rabbit IgG HRP- conjugated	1:10000	#32460	Thermo

646

647 **9. Lactate dehydrogenase (LDH) release cytotoxicity assay.**

648 Apical and basolateral samples were used to quantify LDH release in RV-C15-infected

649 HAE with the CytoTox 96® Non-Radioactive Cytotoxicity Assay kit (#G1780; Promega, Madison,

650 WI) following the manufacturer's protocol.

651

652 **10. Transepithelial Electrical Resistance (TEER) assay.**

653 TEER was quantified in HAE using the Millicell Electrical Resistance System (ERS)-2

654 (Sigma) after adding 100µl of Pneumacult-ALI medium to the apical surface and incubating

655 cultures for 30 minutes at 34°C. Statistical analysis of resulting data was done by ordinary one-

656   way ANOVA and Tukey's multiple comparison test methods using Prism GraphPad v.9 software

657   (GraphPad).

658

659   **11. Quantification of ZO-1 disposition using JAnaP.**

660   Junction coverage and characterization were quantified using the Junction Analyzer

661   Program (JAnaP) as previously described [44-46]. In short, the perimeter of each cell was

662   identified via waypoints in immunofluorescent images of ZO-1. The junctions were isolated from

663   the background using a threshold value of 5-8. Threshold identification is described in the

664   supplement of [44] and in the JAnaP User-Guide available at https://github.com/StrokaLab/JAnaP

665   along with the JAnaP program in its entirety. Junction characterization was performed by

666   calculating the length of each individual junction piece that coincides with the perimeter as well

667   as the relative aspect ratio (RAR) with respect to the cell perimeter. A junction was classified as

668   continuous if its length was greater than 15 pixels, otherwise it was deemed discontinuous and

669   further separated into perpendicular or punctate if the RAR was greater or less than 1.2,

670   respectively. Statistical analysis was done by one-way ANOVA and Dunnett's multiple

671   comparison test using Prism GraphPad v.9 software (GraphPad).

672

673   **12. Measurement of Mucociliary Clearance (MCC).**

674   Mucociliary transport was measured based on the transport of 2µm red-fluorescent

675   polystyrene microspheres (Sigma-Aldrich). Five microliters of microspheres suspension (1:500

676   dilution in PBS; Sigma-Aldrich) was added on top of the native mucus; after 24-hour incubation

677   at 34°C, videos of three regions were recorded using Zeiss Axio Observer 3 Inverted fluorescence

678   microscope (Cell Observer HS image system, Zeiss Axiocam 503 mono camera, optimal

679   acquisition mode, Zen 2007 software) equipped with 10x/0.25NA Ph1 air objective. Images were

680   collected at a frame rate of 0.5 Hz for 10 seconds on the plane of the mucus gel. Images were

681 acquired centrally within cultures and away from the edges, where mucus tends to accumulate.

682 The microsphere tracking data analysis was based on an image processing algorithm that was

683 custom written in MATLAB (The MathWorks). Briefly, the analysis software computes the XY-

684 plane trajectories of each fluorescent microsphere in each frame. Using the trajectory data,

685 displacement of microspheres was computed, and transport rate was calculated by dividing the

686 displacement of microsphere by total time elapsed.

687

Acknowledgments

699

References

701 [1] Eurico Arruda, Anne Pitkaranta, Theodore J. Witek jr, Caroline A. Doyle, Frederick G. Hayden.

702 Frequency and Natural History of Rhinovirus Infections in Adults during Autum. J of Clin Microbiol.

703 1997; 35 (11): 2864–8.

704 [2] Wai-Ming Lee, Robert F. Lemanske Jr, Michael D. Evans, Fue Vang, et al. Human Rhinovirus

705 Species and Season of Infection Determine Illness Severity. Am J Respir Crit Care Med. 2012;

706 186 (9): 886–91. doi: 10.1164/rccm.201202-0330OC

707 [3] Kim T. Ng, Xiang Y. Oong, Sin H. Lim, Jack B. Chook, Yutaka Takebe, et al. Viral Load and

708 Sequence Analysis Reveal the Symptom Severity, Diversity, and Transmission Clusters of

709 Rhinovirus Infections. Clin Infect Dis. 2018; 67 (2): 261–8. doi: 10.1093/cid/ciy063

710 [4] Alessandra K. Matsuno, Talita B. Gagliardi, Flavia E. Paula, Luciano K. S. Luna, Bruna L. S.

711 Jesus, et al. Human coronavirus alone or in co-infection with rhinovirus C is a risk factor for severe

712 respiratory disease and admission to the pediatric intensive care unit: A one-year study in

713 Southeast Brazil. PLoS ONE. 2019; 14 (6): e0217744. doi: 10.1371/journal. pone.0217744

714 [5] Jonathan M Corne, Clare Marshall, Sandra Smith, Jacquie Schreiber, Gwendolyn Sanderson,

715 et al. Frequency, severity, and duration of rhinovirus infections in asthmatic and non-asthmatic

716 individuals: a longitudinal cohort study. The Lancet. 2002; 359: 831–34. doi: 10.1016/S0140-

717 6736(02)07953-9.

718 [6] J. Bizzintino, W-M. Lee, I.A. Laing, F. Vang, T. Pappas, et al. Association between human

719 rhinovirus C and severity of acute asthma in children. Eur Respir J. 2011; 37: 1037–1042. doi:

720 10.1183/09031936.00092410

721 [7] Jie Zhu, Simon D. Message, Yusheng Qiu, Patrick Mallia, Tatiana Kebadze. Airway

722 Inflammation and Illness Severity in Response to Experimental Rhinovirus Infection in Asthma.

723 Chest. 2014; 145 (6): 1219-29. doi: 10.1378/chest.13-1567.

724 [8] Riitta Turunen, Tuomas Jartti, Yury A. Bochkov, James E. Gern, Tytti Vuorinen. Rhinovirus

725 Species and Clinical Characteristics in the First Wheezing Episode in Children. J Med Virol. 2016;

726 88: 2059–68. doi: 10.1002/jmv.24587

727 [9] Peter Simmonds, Chloe L. McIntyre, Carita Savolainen-Kopra, Caroline Tapparel, Ian M.

728 Mackay, et al (2010). Proposals for the classification of human rhinovirus species C into

729 genotypically-assigned types. J Gen Virol. 2010; 91: 2409–19. doi: 10.1099/vir.0.023994-0

730   [10] Chloe L. McIntyre, Nick J. Knowles, Peter Simmonds. Proposals for the classification of

731   human rhinovirus species A, B and C into genotypically assigned types. J Gen Virol. 2013; 94:

732   1791-1806. doi: 10.1099/vir.0.053686-0

733   [11] Wei-Ju Chen, John C. Arnold, Mary P. Fairchok, Patrick J. Danaher, Erin A. McDonough, et

734   al. Epidemiologic, clinical, and virologic characteristics of human rhinovirus infection among

735   otherwise healthy children and adults Rhinovirus among adults and children. J of Clin Virol. 2015;

736   64: 74–82. doi: 10.1016/j.jcv.2015.01.007

737   [12] E. Kathryn Miller, Jodell Linder, David Kraft, Monika Johnson, Pengcheng Lu, et al.

738   Hospitalizations and outpatient visits for rhinovirus-associated acute respiratory illness in adults.

739   J Allergy Clin Immunol. 2015; 137 (3): 734-43. doi: 10.1016/j.jaci.2015.06.017

740   [13] Robert F. Lemanske Jr, Daniel J. Jackson, Ronald E. Gangnon, Michael D. Evans, Zhanhai

741   Li, et al. Rhinovirus illnesses during infancy predict subsequent childhood wheezing. J Allergy

742   Clin Immunol. 2005; 116 (3): 571-7.doi:10.1016/j.jaci.2005.06.024

743   [14] Katarina Stenberg-Hammar, Gunilla Hedlin, Cilla Söderhäll. Rhinovirus and preschool

744   wheeze. Pediatr Allergy Immunol. 2017; 28: 513–20. doi: 10.1111/pai.12740

745   [15] Daryl Lamson, Neil Renwick, Vishal Kapoor, Zhiqiang Liu, Gustavo Palacios, et al. MassTag

746   Polymerase-Chain-Reaction Detection of Respiratory Pathogens, Including a New Rhinovirus

747   Genotype, That Caused Influenza-Like Illness in New York State during 2004–2005. The J of Inf

748   Dis. 2006; 194: 1398–1402. doi: 0022-1899/2006/19410-0008$15.00

749   [16] Ann C. Palmenberg, David Spiro, Ryan Kuzmickas, Shiliang Wang, Appolinaire Djikeng, et

750   al. Sequencing and Analyses of All Known Human Rhinovirus Genomes Reveal Structure and

751   Evolution . Science. 2009; 324 (3): 55-9. doi: 10.1126/science.1165557.

752   [17] Yue Liua, Marchel G. Hillb, Thomas Klosea, Zhenguo Chena, Kelly Watters , et al. Atomic

753   structure of a rhinovirus C, a virus species linked to severe childhood asthma. PNAS. 2016; 113

754   (32); 8997–9002. doi: 10.1073/pnas.1606595113

755   [18] Léna Royston and Caroline Tapparel. Rhinoviruses and Respiratory Enteroviruses: Not as

756   Simple as ABC. Viruses. 2016; 8 (16): 1-23. doi:10.3390/v8010016

757   [19] Yury A. Bochkova, Kelly Watters, Shamaila Ashrafa, Theodor F. Griggs, Mark K. Devries, et

758   al. Cadherin-related family member 3, a childhood asthma susceptibility gene product, mediates

759   rhinovirus C binding and replication. PNAS. 2015; 112 (17): 5485–90. doi:

760   10.1073/pnas.1421178112

761   [20] Klaus Bønnelykke, Patrick Sleiman, Kasper Nielsen, Eskil Kreiner-Møller, Josep M Mercader,

762   et al. A genome-wide association study identifies CDHR3 as a susceptibility locus for early

763   childhood asthma with severe exacerbations. Nature Genetics. 2014; 46 (1): 51-8.

764   doi:10.1038/ng.2830

765   [21] Sarmila Basnet, Yury A. Bochkov, Rebecca A. Brockman-Schneider, Ine Kuipers, Scott W.

766   Aesif, et al. CDHR3 Asthma-Risk Genotype Affects Susceptibility of Airway Epithelium to

767   Rhinovirus C Infections. American Journal of Respiratory Cell and Molecular Biology. 2019; 61

768   (4): 450-8. doi: 10.1165/rcmb.2018-0220OC

769   [22] Theodor F. Griggs, Yury A. Bochkov, Sarmila Basnet, Thomas R. Pasic, Rebecca A.

770   Brockman-Schneider, et al. Rhinovirus C targets ciliated airway epithelial cells. Respiratory

771   Research. 2017; 18: 84. doi: 10.1186/s12931-017-0567-0

772   [23] Jamie L. Everman, Satria Sajuthi, Benjamin Saef, Cydney Rios, Ari M. Stoner, et al.

773   Functional genomics of CDHR3 confirms its role in HRV-C infection and childhood asthma

774   exacerbations. J Allergy Clin Immunol. 2019; 144 (4); 962-71. doi: 10.1016/j.jaci.2019.01.052

775   [24] Kevin L. McKnight, Karen V. Swanson, Kathryn Austgen, Cindy Richards, Jonathan K.

776   Mitchell, et al. Stimulator of interferon genes (STING) is an essential proviral host factor for human

777   rhinovirus species A and C. PNAS. 2020; 117 (44): 27598-27607. doi: 10.1073/pnas.2014940117

778   [25] Shamaila Ashrafa, Rebecca Brockman-Schneidera, Yury A. Bochkova, Thomas R. Pasicb,

779   James E. Gern. Biological Characteristics and Propagation of Human Rhinovirus–C in

780 Differentiated Sinus Epithelial Cells. Virology. 2013; 436 (1): 143–9.

781 doi:10.1016/j.virol.2012.11.002

782 [26] Weidong Hao, Katie Bernard, Nita Patel, Nancy Ulbrandt, Hui Feng, et al. Infection and

783 Propagation of Human Rhinovirus C in Human Airway Epithelial Cells. J of Virol. 2012; 86 (24):

784 13524–13532 doi: 10.1128/JVI.02094-12

785 [27] Caroline Tapparel, Komla Sobo, Samuel Constant, Song Huang, Sandra Van Belle, et al.

786 Growth and characterization of different human rhinovirus C types in three-dimensional human

787 airway epithelia reconstituted in vitro. Virology. 2013; 446: 1–8. doi: 10.1016/j.virol.2013.06.031

788 [28] George A. Belov, Vinod Nair, Bryan T. Hansen, Forrest H. Hoyt, Elizabeth R. Fischer, et al.

789 Complex Dynamic Development of Poliovirus Membranous Replication Complexes. J of Virol.

790 2011; 86 (1): 302–12. doi: 10.1128/JVI.05937-11

791 [29] Hyung S. Oh, Sravani Banerjee, David Aponte-Diaz, Suresh D. Sharma, Jason Aligo, et al.

792 Cameron. Multiple poliovirus-induced organelles suggested by comparison of spatiotemporal

793 dynamics of membranous structures and phosphoinositides. PLoS Pathogens. 2018; 14 (4):

794 e1007036. doi: 10.1371/journal.ppat.1007036

795 [30] Sravani Banerjee, David Aponte-Diaz, Calvin Yeager, Suresh D. Sharma, Gang Ning, et al.

796 Hijacking of multiple phospholipid biosynthetic pathways and induction of membrane biogenesis

797 by a picornaviral 3CD protein. PLoS Pathogens. 2018; 14 (5): e1007086. doi: 10.1371/journal.

798 ppat.1007086

799 [31] Pascal S. Roulin, Mark Lotzerich, Federico Torta, Lukas B. Tanner, Frank J.M. van

800 Kuppeveld, et al. Rhinovirus Uses a Phosphatidylinositol 4-Phosphate/Cholesterol Counter-

801 Current for the Formation of Replication Compartments at the ER-Golgi Interface. Cell Host &

802 Microbe. 2014; 16: 677–690. doi: 10.1016/j.chom.2014.10.003

803 [32] Robert R Dourmashkin, Glynis Dunn, Victor Castano and Sherman A McCall. Evidence for

804 an enterovirus as the cause of encephalitis lethargica. BMC Infectious Diseases. 2012; 12: 136-

805 56. doi: 1471-2334/12/136

806 [33] Cythia S. Goldsmith and Yiting Zhang. Particles of the EV-D68 virus. CDC. Available

807 from:https://commons.wikimedia.org/wiki/File:Ev-d68-photo-1.jpg

808 [34] Claire A. Quiner , William T. Jackson. Fragmentation of the Golgi apparatus provides

809 replication membranes for human rhinovirus 1A. Virology. 2010; 407: 185–195. doi:

810 10.1016/j.virol.2010.08.012

811 [35] Aurelie Mousnier, Dawid Swieboda, Anaïs Pinto, Anabel Guedán, Andrew V. Rogers, et al.

812 Human Rhinovirus 16 Causes Golgi Apparatus Fragmentation without Blocking Protein Secretion.

813 J of Virol. 2014; 88 (20): 11671-85. doi: 10.1128/JVI.01170-14

814 [36] Els Wessels, Dani ̈el Duijsings, Kjerstin H. W. Lanke, Sander H. J. van Dooren, Catherine L.

815 Jackson, et al. Effects of Picornavirus 3A Proteins on Protein Transport and GBF1-Dependent

816 COP-I Recruitment. J of Virol. 2006; 80 (23): 11852–60. doi:10.1128/JVI.01225-06

817 [37] Ying-Han Chen, WenLi Du, Marne C Hagemeijer, Peter M Takvorian, Cyrilla Pau, et al.

818 Phosphatidylserine vesicles enable efficient en bloc transmission of multiple enteroviruses. Cell.

819 2015; 160 (4): 619–30. doi:10.1016/j.cell.2015.01.032.

820 [38] William T. Jackson, Thomas H. Giddings Jr., Matthew P. Taylor, Sara Mulinyawe, Marlene

821 Rabinovitch, et al. Subversion of Cellular Autophagosomal Machinery by RNA Viruses. PLoS Biol.

822 2005; 3 (5): e156. doi: 10.1371/journal.pbio.0030156

823 [39] Kathryn A Klein and William T Jackson. Human Rhinovirus 2 Induces the Autophagic

824 Pathway and Replicates More Efficiently in Autophagic Cells. J of Virol. 2011; 85 (18): 9651–4.

825 doi:10.1128/JVI.00316-11

826 [40] Abigail K Corona, Holly M Saulsbery, Angel F Corona Velazquez, William T Jackson.

827 Enteroviruses Remodel Autophagic Trafficking through Regulation of Host SNARE Proteins to

828 Promote Virus Replication and Cell Exit. Cell Reports. 2018; 22: 3304–14. doi:

829 10.1016/j.celrep.2018.03.003

830 [41] Qingyuan Zhu, Hui Hu, Haixia Liu, Hong Shen, Zhipeng Yan, et al. A synthetic STING agonist

831 inhibits the replication of human parainfluenza virus 3 and rhinovirus 16 through distinct

832 mechanisms. Antiviral Research. 2020; 183: 104933. doi: 10.1016/j.antiviral.2020.104933

833 [42] Walters MS, Gomi K, Ashbridge B, Moore MAS, Arbelaez V, et al. Generation of a human

834 airway 797 epithelium derived basal cell line with multipotent differentiation capacity. Respir Res.

835 2013; 14: 135. doi: 10.1186/1465-9921-14-135

836 [43] Oscar R Colegio, Christina V Itallie, Christophe Rahne, James M Anderson. Claudin

837 extracellular domains determine paracellular charge selectivity and resistance but not tight

838 junction fibril architecture. Am J Physiol Cell Physiol. 2003; 284 (6): C1346-54. doi:

839 10.1152/ajpcell.00547.2002.

840 [44] Kelsey M Gray, Dakota B Katz, Erica G Brown, Kimberly M Stroka. Quantitative Phenotyping

841 of Cell–Cell Junctions to Evaluate ZO-1 Presentation in Brain Endothelial Cells. Annals of

842 Biomedical Engineering. 2019; 47 (7): 1675-87. doi: 10.1007/s10439-019-02266-5

843 [45] Marina A Pranda, Kelsey M. Gray, Ariana Joy L. DeCastro, Gregory M. Dawson, Jae W. Jung,

844 et al. Tumor Cell Mechanosensing During Incorporation into the Brain Microvascular Endothelium.

845 Cell Mol Bioeng. 2019; 12 (5): 455-80. doi: 10.1007/s12195-019-00591-2

846 [46] Kelsey M Gray, Jae W Jung, Collin T Inglut, Huang-Chiao Huang, Kimberly M Stroka.

847 Quantitatively relating brain endothelial cell-cell junction phenotype to global and local barrier

848 properties under varied culture conditions via the Junction Analyzer Program. Fluids Barriers CNS.

849 2020; 17 (1): 16. doi: 10.1186/s12987-020-0177-y

850 [47] Renate Fuchs and Dieter Blaas. Uncoating of human rhinoviruses Rev Med Virol. 2010; 20:

851 281–97. doi: 10.1002/rmv.654

852 [48] Birgit Winther, Eurico Arruda, Theodore J. Witek, Steven D. Marlin, Michael M. Tsianco, et

853 al. Expression of ICAM-1 in Nasal Epithelium and Levels of Soluble ICAM-1 in Nasal Lavage Fluid

854 During Human Experimental Rhinovirus Infection. Arch Otolaryngol Head Neck Surg. 2002; 128:

855 131-6. doi: 10.1001/archotol.128.2.131.

856 [49] Alberto Papi and Sebastian L. Johnston. Rhinovirus Infection Induces Expression of Its Own

857 Receptor Intercellular Adhesion Molecule 1 (ICAM-1) via Increased NF-kb mediated Transcription.

858 The J of Biol Biochem. 1999; 274 (14): 9707–20. doi: 10.1074/jbc.274.14.9707.

859 [50] Tomoko Suzuki, Mutsuo Yamaya, Masahito kamanaka, Yu X. Jia, Katsutoshi Nakayama, et

860 al. Type 2 rhinovirus infection of cultured human tracheal epithelial cells: role of LDL receptor. Am

861 J Physiol Lung Cell Mol Physiol. 2001; 280: L409–L420. doi: 10.1152/ajplung.2001.280.3.L409

862 [51] David A Suhy, Thomas H Giddings Jr, Karla Kirkegaard. Remodeling the endoplasmic

863 reticulum by poliovirus infection and by individual viral proteins: an autophagy-like origin for virus-

864 induced vesicles. J of Virol. 2000; 74 (19): 8953–65. doi; 0022-538x/00/$04.00+0

865 [52] Denise Egger and Kurt Bienz. Intracellular location and translocation of silent and active

866 poliovirus replication complexes. J of Gen Virol. 2005; 86: 707–18. doi: 10.1099/vir.0.80442-0

867 [53] Aline Schögler, Oliver Caliaro, Melanie Brügger, Blandina I. Oliveira Esteves, Izabela Nita, et

868 al. Modulation of the unfolded protein response pathway as an antiviral T approach in airway

869 epithelial cells. Antiviral Research. 2019; 162: 44–50. doi: 10.1016/j.antiviral.2018.12.007

870 [54] Juan Song, Miaomiao Chi, Xiaonuan Luo, Qinqin Song, Dong Xia, et al. Non-Structural

871 Protein 2B of Human Rhinovirus 16 Activates Both PERK and ATF6 Rather Than IRE1 to Trigger

872 ER Stress. Viruses. 2019; 11 (133): 1-17.doi:10.3390/v11020133

873 [55] Frank JM van Kuppeveld, Joost GJ Hoenderop, Rolf LL Smeets, Peter HGM Willems,

874 Henri BPM Dijkman, et al. Coxsackievirus protein 2B modifies endoplasmic reticulum membrane

875 and plasma membrane permeability and facilitates virus release. The EMBO Journal. 1997; 16

876 (12): 3519–32. doi: 10.1093/emboj/16.12.3519

877 [56] Jianjun Wu, Yu-Ju Chen, Nicole Dobbs, Tomomi Sakai, Jen Liou, et al. STING-mediated

878 disruption of calcium homeostasis chronically activates ER stress and primes T cell death. J Exp

879 Med. 2019; 216 (4): 867–83. doi:10.1084/jem.20182192

880   [57] Dongshan Wan, Wei Jiang, and Junwei Hao. Research Advances in How the cGAS-STING

881   Pathway Controls the Cellular Inflammatory Response. Research Advances in How the cGAS-

882   STING Pathway Controls the Cellular Inflammatory Response. Front Immunol. 2020; 11: 615. doi:

883   10.3389/fimmu.2020.00615

884   [58] Umadevi Sajjan, Qiong Wang, Ying Zhao, Dieter C. Gruenert, Marc B. Hershenson.

885   Rhinovirus Disrupts the Barrier Function of Polarized Airway Epithelial Cells. Am J Respir Crit

886   Care Med. 2008; 178: 1271-81. doi: 10.1164/rccm.200801-136OC

887   [59] Carolyn B Coyne, Todd M Gambling, Richard C Boucher, Johnny L Carson, Larry G Johnson.

888   Role of claudin interactions in airway tight junctional permeability. Am J Physiol Lung Cell Mol

889   Physiol. 2003; 285: L1166–L1178. doi:10.1152/ajplung.00182.2003.

890   [60] Carolyn B Coyne, Miriam K Vanhook, Todd M Gambling, Johnny L Carson, Richard C

891   Boucher, et al.Regulation of Airway Tight Junctions by Proinflammatory Cytokines. Mol Biol of the

892   Cell. 202; 13: 3218–34. doi:10.1091/mbc.E02– 03– 0134.

893   [61] Ceniz Zihni, Clare Mills, Karl Matter, Maria S. Balda. Tight junctions: from simple barriers to

894   multifunctional molecular gates. Nature reviews. 2016; 17: 564-80. doi:10.1038/nrm.2016.80

895   [62] Manel Essaidi-Laziosi, Francisco Brito, Sacha Benaoudia, Lena Royston, Samuel Constant,

896   et al. Propagation of respiratory viruses in human airway epithelia reveals persistent virus-specific

897   signatures. J Allergy Clin Immunol. 2018;141 (6): 2074-84. doi: 10.1016/j.jaci.2017.07.018

898   [63] Ximena M. Bustamante-Marin and Lawrence E. Ostrowski. Cilia and Mucociliary Clearance.

899   Cold Spring Harb Perspect Biol. 2017; 9: a028241. doi: 10.1101/cshperspect.a028241

900   [64] Marrah E. Lachowicz-Scroggins, Homer A. Boushey, Walter E. Finkbeiner, Jonathan H.

901   Widdicombe. Interleukin-13–Induced Mucous Metaplasia Increases Susceptibility of Human

902   Airway Epithelium to Rhinovirus Infection. Am J Respir Cell Mol Biol. 2010; 43. 652–61. doi:

903   10.1165/rcmb.2009-0244OC

904 [65] Jamila Laoukili, Eric Perret, Tom Willems, Adrian Minty, Eef Parthoens, et al. IL-13 alters

905 mucociliary differentiation and ciliary beating of human respiratory epithelial cells. The J of Clini

906 Investigation. 2001; 108 (12): 1817-24. doi: 10.1172/JCI200113557.

907 [66] Atsushi Yuta, William J Doyle, Ethan Gaumond, Mushtaq Ali, Lawrence Tamarkin, et al.

908 Rhinovirus infection induces mucus hypersecretion. Am J Physiol. 1998; 274 (18): L1017– L1023.

909 Doi: 10.1152/ajplung.1998.274.6.L1017.

910 [67] Shao-heng He, Jian Zheng, Ming-ke Duan. Induction of mucin secretion from human

911 bronchial tissue and epithelial cells by rhinovirus and lipopolysaccharide. Acta Pharmacol Sin.

912 2004; 25 (9): 1176-81.

913 [68] Wai-Ming Lee, Wensheng Wang, Yury A Bochkov, Iris Lee. Reverse Genetics System for

914 Studying Human Rhinovirus Infections. Methods Mol Biol. 2015; 1221: 149–70. doi:10.1007/978-

915 1-4939-1571-2_12.

916 [69] Theodor F Griggs, Yury A Bochkov, Kazuyuki Nakagome, Ann C Palmenberg, James E Gern.

917 Production, purification, and capsid stability of rhinovirus C types. J of Virol Methods. 2015; 217:

918 18–23. doi: 10.1016/j.jviromet.2015.02.019

919 [70] Neville E Sanjana, Ophir Shalem, Feng Zhang. Improved vectors and genome-wide libraries

920 for CRISPR screening. Nat Methods. 2014; 11 (8): 783-4. doi: 10.1038/nmeth.3047

921 [71] Sheila A Stewart, Derek M Dykxhoorn, Deborah Palliser, Hana Mizuno H, Evan Y Yu , et al.

922 Lentivirus-delivered stable gene silencing by 850 RNAi in primary cells. RNA. 2003; 9 (4): 493–

923 501. doi: 10.1261/rna.2192803.

924 [72] Milan Fiala. Plaque Formation by 55 Rhinovirus Serotypes. Applied Microbiol. 1968; 16 (10):

925 1445-50.

926 [73] Johannes Schindelin, Ignacio Arganda-Carreras, Erwin Frise, Verena Kaynig,

927 Mark Longair, et al. Fiji: an open-source platform for biological-image analysis. Nature methods.

928 2012; 9 (7): 676-82. doi: 10.1038/nmeth.2019

929   [74] Luke Hammond. Corrected Total Cell Fluorescence (CTCF). The University of Queensland,

930   Australia.   Available   from: https://theolb.readthedocs.io/en/latest/imaging/measuring-cell-

931   fluorescence-using-imagej.html

932   [75] Susanne Bolte, Fabrice P. Cordelieres. A guided tour into subcellular colocalization analysis

933   in   light   microscopy.   J   of   Microscopy.   2006;   224   (3):   213-32.   doi: 10.1111/j.1365-

934   2818.2006.01706.x

935

936   **Figure captions**

937   **Figure 1. RV-C15 replicates in ciliated epithelial cells, leading to decreased CDHR3 levels.**

938   **A and B:** Multi-cycle RV-C15 growth delineated at 34°C in HAE (**A:** donor 1; **B:** donor 2). **C-E:**

939   Immunofluorescence detection of CDHR3 (red) in non-infected or RV-C15-infected (dsRNA+;

940   gray) ciliated cells identified by either acetylated α-tubulin (green; **C and D**) or FoxJ1 (green; **E**)

941   at 12 hpi. **C:** scale bar = 10μm. **D and E:** 3D visualization; z-stacks were at 1μm of thickness. **F:**

942   Immunofluorescence detection of RV-C15 replication (dsRNA; red) in ciliated cells (FoxJ1, gray)

943   with/or without motile cilia (acetylated α-tubulin, green) at 12 hpi (scale bar = 10μm). **G:**

944   Quantification of dsRNA and CDHR3 fluorescence levels (CTCF) in non-infected (N) and RV-

945   C15-infected (C15; dsRNA+) ciliated cells following immunofluorescence staining at 12 hpi.

946   Graphs show dsRNA and CDHR3 total CTCF (line = mean) quantified in HAE using FoxJ1 (N(1)

947   and C15(1)) or acetylated α-tubulin (C15(2) and N(2)) as a marker of ciliated cells. Statistical

948   analysis was done using the Mann-Whitney U test (Two-tailed; 0.95% confidence interval;

949   *p<0.05, ***p<0.001, ****p<0.0001).

950

951   **Figure 2. Detection of RV-C15 replication complexes in HAE**. **A-C:** Orthogonal views (XY, XZ

952   and YZ planes; yellow lines show the location of XZ and YZ views on the XY plane) from non-

953   infected **(A)** and RV-C15-infected (**B-C**) cells immunostained for dsRNA (red) and nuclei (blue) at

954   12 hpi (z-stacks at 1μm of thickness; scale bar = 10μm). **B-C**: Z-stacks (1μm of thickness) from

955   RV-C15-infected HAE show dsRNA (red) detection by immunofluorescence with perinuclear **(B)**

956   or "ring-like" disposition close to the plasma membrane (**C**). **D-E:** TEM of non-infected (**D**) and

957   RV-C15-infected (**E**) HAE fixed at 12 hpi (scale bar = 5μm). **D:** Visualization of ciliated cells *(CC)*

958   in non-infected HAE (**D –** *left panel)* occasionally revealed small vesicles spread through the

959   cytoplasm *(**D** – right panel*). **E:** Larger vesicles were detected in ciliated cells (*CC*) from RV-C15-

960   infected HAE that resembled 'replicative complexes' (*RC*; **E** – *upper-left panel*) observed during

961   RV-A and RV-B infection [30]. These vesicles were detected in close proximity to mitochondria

962   (*Mt*) and multi-vesicular bodies (*MVB*; **E** – *upper-right panel*), and were found to have double-

963   membranes (DMV; **E** – *lower-left panel*). Clusters of electron-dense structures in the cytoplasm

964   of RV-C15-infected HAE were seen, reminiscent of viral crystals (VC; **E** – *lower-right panel*)

965   described for other picornaviruses [32, 33]. Glyc = glycogen.

966

967   **Figure 3. Neither the Golgi nor PI4P-positive vesicles are the main site for RV-C15**

968   **replication in HAE. A**: Visualization of giantin (Golgi marker, green; nuclei, blue) in non-infected

969   HAE and in HAE infected with RV-C15, RV-A16, or RV-A2 (dsRNA+, red) by immunofluorescence

970   (z-stacks at 1μm of thickness; scale bar = 10μm) at 12hpi. **B:** Golgi stacks observed by TEM in

971   ciliated cells from non-infected (*left panel*) and RV-C15-infected HAE (*right panel*) at 12 hpi (scale

972   bar = 2μm). **C**: 3D view of PI4P (green) and giantin (gray) in non-infected or rhinovirus-infected

973   (dsRNA+, red) HAE (nuclei, blue) detected by immunofluorescence at 12hpi (z-stacks at 1μm of

974   thickness). **D:** Quantification of fluorescence levels (CTCF; line = mean) of dsRNA, giantin, and

975   PI4P in non-infected HAE and HAE infected with RV-C15, RV-A16, or RV-A2 (dsRNA+ cells) at

976   12 hpi. Statistical analysis was done using the Kruskal-Wallis test following Dunn's multi-

977   comparison test (*$p<0.05$, **$p<0.01$, ***$p<0.001$, ****$p<0.0001$; ns = non-significant). **E:** Spearman

978   correlation analysis (two-tailed; 0.95% confidence interval) between PI4P and giantin

979   fluorescence levels (CTCF) and also between each protein and dsRNA in RV-C15-infected HAE

980   at 12hpi. **F and G:** 3D surface plot of RV-C15-infected HAE (at 12hpi) showing the

981   immunodetection of dsRNA (red; **F and G**), giantin (green; **F**), PI4P (green; **G**); and colocalization

982   (yellow) between dsRNA/giantin (**F**) or dsRNA/PI4P (**G**). **H and I**: Spatial colocalization analysis

983   of dsRNA/giantin (**H**) and dsRNA/PI4P (**I**) in HAE infected with RV-C15, RV-A16, and RV-A2 at

984   12 hpi. The median colocalization ratio is noted on top of each bar. Statistical analysis was done

985   by Kruskal-Wallis test following Dunn's multi-comparison test.

986

987   **Figure 4. ER is a site for RV-C15 genome replication in HAE. A**: Detection of calnexin (ER

988   marker, green; nuclei, blue) in non-infected or rhinovirus-infected (dsRNA+, red) HAE at 12 hpi

989   (z-stacks at 1µm of thickness; scale bar = 5µm). **B:** Quantification of fluorescence levels (CTCF;

990   line = mean) of dsRNA and calnexin in non-infected cells and RV-infected (dsRNA+) HAE

991   detected by immunofluorescence at 12 hpi. Statistical analysis was done using Kruskal-Wallis

992   test following Dunn's multi-comparison test (**p<0.01, **** p<0.0001). **C:** Spearman correlation

993   analysis (two-tailed; 0.95% confidence interval) between calnexin and dsRNA fluorescence levels

994   (CTCF) in RV-C15, -A16, or -A2-infected HAE at 12 hpi. **D:** 3D view of RV-C15-infected HAE

995   shows the immunodetection of calnexin (green), viral dsRNA (red), and calnexin/dsRNA

996   colocalization (yellow and orange) at 12 hpi (z-stacks at 1µm of thickness). **E:** 3D surface plot of

997   RV-C15-infected HAE shows the detection of calnexin (green), dsRNA (red), and calnexin/dsRNA

998   colocalization (yellow) by immunofluorescence at 12 hpi. **F-G:** Spatial colocalization analysis done

999   in RV-C15, RV-A16, or RV-A2-infected HAE (dsRNA+) shows the ratio of dsRNA/calnexin (**F**) and

1000   calnexin/dsRNA (**G**) colocalization at 12 hpi. The median colocalization ratio is plotted on top of

1001   each bar; statistical analysis was done by Kruskal-Wallis test following Dunn's multi-comparison

1002   test (*p<0.05; ** p<0.01).

1003

1004   **Figure 5. RV-C15 replication induces incomplete autophagy in HAE at 12 hpi. A:** Fold

1005   change graph represents Lamp1, LC3b-I, and LC3b-II protein levels normalized to the

1006 endogenous control (actin) and compared to non-infected cultures. Data shown are from two

1007 independent donors, represented by circles and triangles. Blot below is from the donor

1008 represented by circles. **B:** Detection of Lamp-1 (gray), LC3b (green) and dsRNA (red; nuclei, blue)

1009 in non-infected HAE and HAE infected with RV-C15, RV-A16, or RV-A2 by immunofluorescence

1010 at 12 hpi (z-stacks at 1μm of thickness; scale bar = 5μm). **C:** Quantification of fluorescence levels

1011 (CTCF) for Lamp-1, LC3b, and dsRNA in non-infected and RV-infected (dsRNA+) HAE at 12 hpi.

1012 Statistical analysis was done by Kruskal-Wallis test following Dunn's multi-comparison test

1013 (*$p<0.05$, **$p<0.01$, ***$p<0.001$, ****$p<0.0001$, ns = non-significant). **D:** Spearman correlation

1014 analysis (two-tailed; 0.95% confidence interval) between fluorescence levels for dsRNA and

1015 Lamp-1 or LC3b in RV-C15-infected HAE at 12 hpi. **E:** Spatial colocalization analysis of Lamp-

1016 1/LC3b colocalization in RV-C15, RV-A16 and RV-A2 -infected (dsRNA+) HAE at 12hpi. The

1017 median colocalization ratio value is plotted on top of each bar; statistical analysis done by Kruskal-

1018 Wallis test following Dunn's multi-comparison test (*$p<0.05$; ** $p<0.01$).

1019

1020 **Figure 6. STING expression promotes RV-C15 replication in HAE at 12 hpi. A:** Western blot

1021 showing STING expression at 48hpi in non-infected or RV-C15-infected HAE. **B:**

1022 Immunofluorescence detection of STING (green) in non-infected or RV-C15-infected (dsRNA; red)

1023 ciliated cells (acetylated α-tubulin, magenta) at 12 hpi (scale bar = 50μm). **C:** 3D view of RV-C15-

1024 infected HAE shows the detection of STING (green) and viral dsRNA (red) in ciliated cells

1025 (acetylated α-tubulin, gray) at 12 hpi (z-stacks at 1μm of thickness). **D:** Quantification of dsRNA

1026 and STING fluorescence levels (CTCF) in non-infected and RV-C15-infected (dsRNA+) HAE at

1027 12 hpi. Statistical analysis was done by Mann-Whitney test (two-tailed; 0.95% confidence interval;

1028 ****$p<0.0001$). **E:** Spearman correlation analysis (two-tailed; 0.95% confidence interval) between

1029 fluorescence levels for dsRNA and STING in RV-C15-infected HAE at 12 hpi. **F:** 3D surface plot

1030 of RV-C15-infected HAE shows the detection of STING (green), dsRNA (red), and STING/dsRNA

1031 colocalization (yellow and orange) by immunofluorescence at 12 hpi. **G:** Spatial colocalization

42

1032   analysis shows the ratio of dsRNA/STING colocalization in RV-C15-infected HAE at 12 hpi (bar

1033   = median). **H:** Western blot showing the STING expression in HAE derived from BCi-NS1.1 cells

1034   transduced with non-targeting control (NTC), sgRNA1 (sg1), or sgRNA2 (sg2). **I:**

1035   Immunofluorescence detection of dsRNA (red) in HAE derived from BCi-NS1.1 cells transduced

1036   with NTC, sgRNA1 (sg1), or sgRNA2 (sg2) infected with RV-C15, RV-A16, or RV-B14 at 12 hpi

1037   (scale bar = 100μm). **J:** qPCR to detect RV RNA in HAE derived from BCi-NS1.1 cells transduced

1038   with NTC, sgRNA1 (sg1), or sgRNA2 (sg2) and infected with RV-C15, RV-A16, or RV-B14 at 4

1039   and 12 hpi. The black line represents the limit of detection (RV-C15 = $10^{3.5}$; RV-A16 = $10^{5.9}$ (not

1040   visible on the graph); RV-B14=$10^{4.8}$); statistical analysis was done by Ordinary One-way ANOVA

1041   and Tukey's multiple comparisons test (**$p<0.01$).

1042

1043   **Figure 7. RV-C15 infection promotes translocation of tight junction proteins and impairs**

1044   **mucociliary clearance (MCC). A:** Percentage of maximum LDH release graph shows the

1045   cytotoxicity of RV-C15 infection in HAE from two donors (continuous and dash lines). **B:**

1046   Quantification of transepithelial electrical resistance (TEER) in non-infected and RV-C15-infected

1047   HAE (two donors; each performed in triplicate). Statistical analysis was done by Ordinary one-

1048   way ANOVA following Tukey's multiple comparisons test (*$p<0.05$). **C**: Fold change graph

1049   represents claudin-1 and zona occludens-1 (ZO-1) α+ and α- protein levels normalized to the

1050   endogenous control (actin) and compared to non-infected cultures. Data shown are from two

1051   independent donors, represented by circles and squares. Blot below is from the donor

1052   represented by squares; black line represents lanes not included in this analysis. **D-E:**

1053   Visualization of claudin-1 (**D,** gray) and ZO-1 (**E,** gray) in non-infected and RV-C15-infected

1054   (dsRNA+, red) HAE (nuclei, blue) detected by immunofluorescence at 12 hpi (z-stacks at 1μm of

1055   thickness; scale bar = 5μm). **F-I:** Quantification of ZO-1, detected by immunofluorescence, in non-

1056   infected and RV-C15-infected using the JAnaP software [44-46]. Total ZO-1 detected per cell

1057   perimeter (percentage of coverage; **F**); detection of discontinuous ZO-1 (disrupted; **G**) -

1058   perpendicular (**H**) and punctate (**I**) profiles. Statistical analysis was done by Ordinary one-way

1059   ANOVA following Dunnett's multiple-comparison test (*p<0.05, ****p<0.0001). **J:** Mucociliary

1060   clearance (MCC) quantified in non-infected HAE (negative control) and HAE inoculated with either

1061   UV-RV-C15 or RV-C15 (10^{10} RNA). Statistical analysis was done by Ordinary one-way ANOVA

1062   following Dunnett's multiple-comparison test (*p<0.05, ***p<0.001, ****p<0.0001).

1063

1064   ## Supporting figure captions

1065   **S1 Figure. RV-C15 replicates in ciliated epithelial cells, leading to decreased CDHR3 levels.**

1066   **A**: Immunofluorescence to detect dsRNA (red) in RV-C15 (10^{10} RNA) infected HAE (nuclei, blue;

1067   scale bar = 50μm). **B-C**: Spearman correlation analysis (two-tailed; 0.95% confidence interval)

1068   between fluorescence levels of CDHR3 and FoxJ1 (**B**) or acetylated α-tubulin (**C**) in non-infected

1069   HAE at 12 hpi. **D**: Orthogonal XY view from non-infected and RV-C15-infected (dsRNA+, red)

1070   HAE (nuclei, blue) stained by immunofluorescence for FoxJ1 (gray) and acetylated α-tubulin

1071   (green) at 12 hpi (z-stacks at 1μm of thickness; scale bar = 5μm). **E-F:** Fold change graph

1072   represents FoxJ1 (**E**), acetylated α-tubulin (**E**), and CDHR3 (**F**) protein levels normalized to the

1073   endogenous control (actin) and compared to non-infected cultures. Data shown are from two

1074   independent donors, represented by circles and triangles. Blot below is from the donor

1075   represented by circles (**E**) and triangles (**F**). **G-H**: Quantification of fluorescence levels (CTCF) for

1076   FoxJ1 (**G**) and acetylated α-tubulin (**H**) in non-infected and RV-C15-infected (dsRNA+) HAE at 12

1077   hpi. Statistical analysis was done using Mann-Whitney U test (Two-tailed; 0.95% confidence

1078   interval).

1079

1080   **S2 Figure. "Ring-like" dsRNA localization in HAE is not specific to RV-C15 infection. A-D**:

1081   Orthogonal views (XY, XZ and YZ planes; yellow lines show the location of XZ and YZ views on

1082   the XY plane) from the RV-A16 **(A-B)** and RV-A2 (**C-D**) -infected HAE immunostained for dsRNA

1083   (red; nuclei, blue) at 12 hpi (z-stacks at 1µm of thickness). Z-stacks at 1µm of thickness shows

1084   two profiles for dsRNA (red) detection by immunofluorescence at perinuclear (**A, C**) or close to

1085   the plasma membrane in a "ring-like" disposition (**B, D**) at 12 hpi (scale bar = 10µm). **E-F:**

1086   Transmission electron microscopy of HAE infected with RV-A16 (**E**) or RV-A2 (**F**) at 12 hpi (scale

1087   bar = 5µm). Visualization of ciliated cells *(CC)* with large, double-membrane vesicles (DMV; **E**

1088   **and F**) located above (**E –** *left panel)* or below the nucleus (**E –** *middle panel*); and the fusion of

1089   small vesicles to the big ones (**E –** *right panel; yellow arrow).* N = nucleus; GoI = golgi; ER =

1090   endoplasmic reticulum; Aut = autophagosome.

1091

1092   **S3 Figure. Neither the Golgi nor PI4P-positive vesicles are the main site for RV-C15**

1093   **replication in HAE. A-B:** Spearman correlation analysis (two-tailed; 0.95% confidence interval)

1094   between giantin and PI4P fluorescent levels (CTCF) in RV-A16 (**A**) or RV-A2 (**B**) -infected HAE

1095   at 12 hpi.

1096

1097   **S4 Figure. Global calnexin expression is not altered during RV-C15 infection in HAE.** Fold

1098   change graph represents calnexin protein levels normalized to the endogenous control (actin)

1099   and compared to non-infected cultures. Data shown are from two independent donors,

1100   represented by circles and triangles. Blot below is from the donor represented by triangles.

1101

1102   **S5 Figure. RV-C15 replication induces incomplete autophagy in HAE at 12 hpi. A-B:**

1103   Spearman correlation analysis (two-tailed; 0.95% confidence interval) between dsRNA and

1104   Lamp-1 or LC3b fluorescent levels (CTCF) in RV-A16 (**A**) or RV-A2 (**B**) -infected HAE at 12 hpi.

1105

1106   **S6 Figure. Detection of dsRNA in RV-C15, but not UV-RV-C15, inoculated HAE used in the**

1107   **MCC experiment.** Immunofluorescence detection of dsRNA (red; nuclei, blue) in non-infected

1108   HAE or inoculated with UV- RV-C15 or RV-C15 at 12 hpi (scale bar = 10µm).

1109

Funding

1119

Competing interests

1121 The authors have declared that no competing interests exist.

1122

Author contributions

1124 TBG contributed to conceptualization and design of the study, as well as execution and analysis

1125 of the experiments. MEG developed HAE cultures with modified STING expression and analyzed

1126 rhinovirus infection in these cultures. DS performed and analyzed MCC experiments. KMG and

1127 JWJ evaluated ZO-1 disposition using the JANaP software. KMS validated JANaP results and

1128 contributed expertise. GAD validated MCC data and contributed expertise. MAS contributed to

1129 the study design and obtained funding. TBG and MAS wrote the manuscript. All authors reviewed

1130 and approved the final manuscript.

Figures
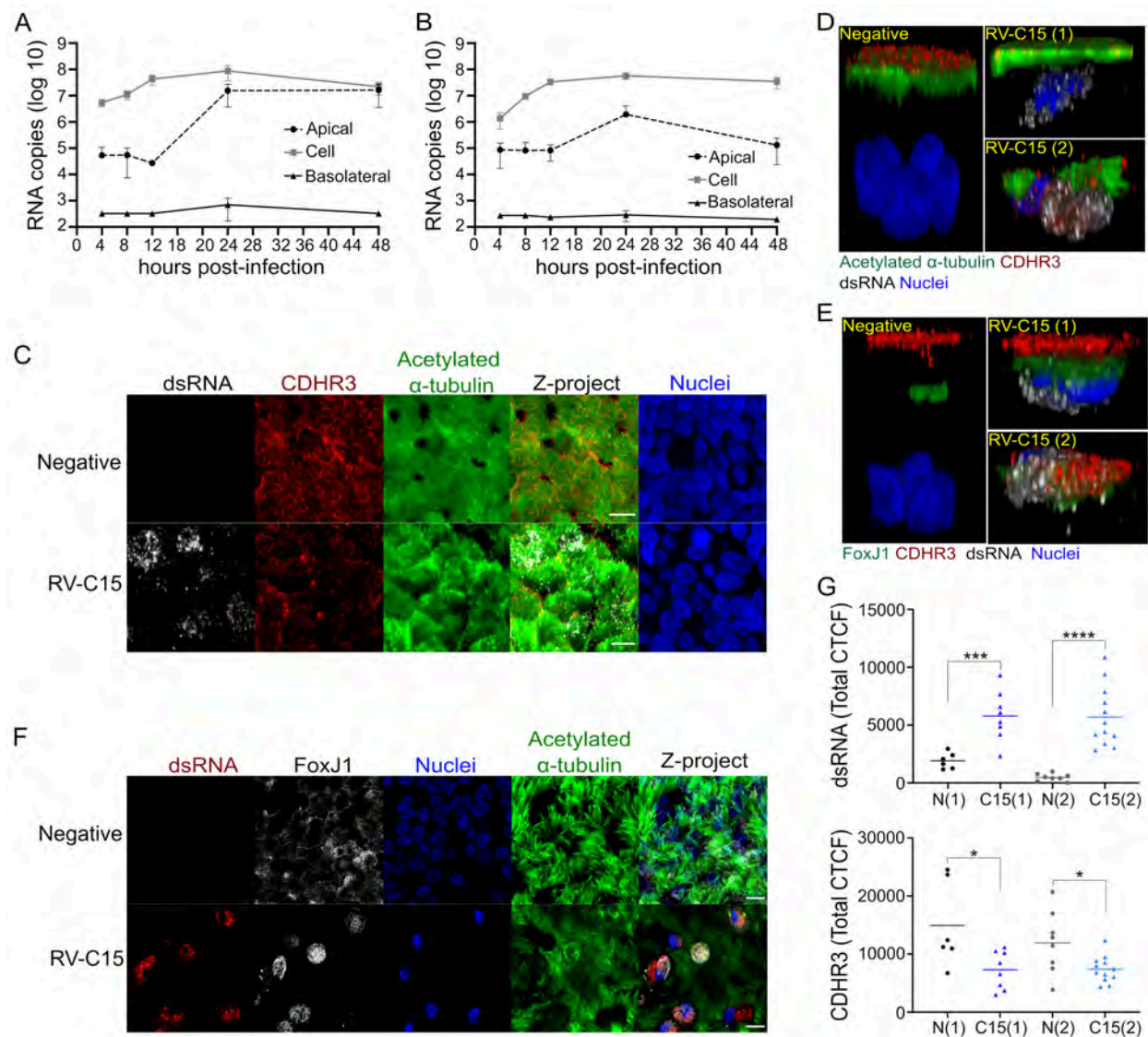
Figure 1. RV-C15 replicates in ciliated epithelial cells, leading to decreased CDHR3 levels.
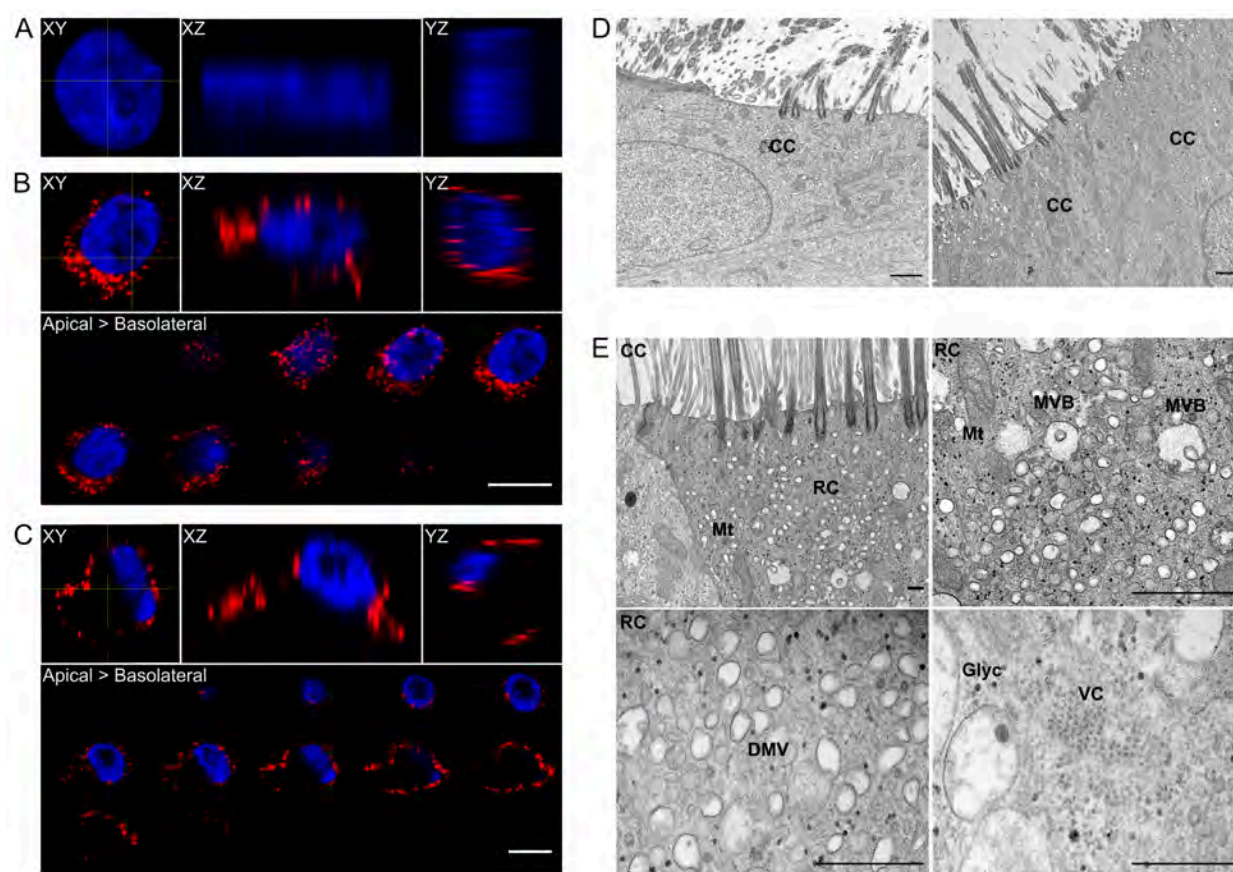
Figure 2. Detection of RV-C15 replication complexes in HAE.

Figure 3. Neither the Golgi nor PI4P-positive vesicles are the main site for RV-C15 replication in HAE.
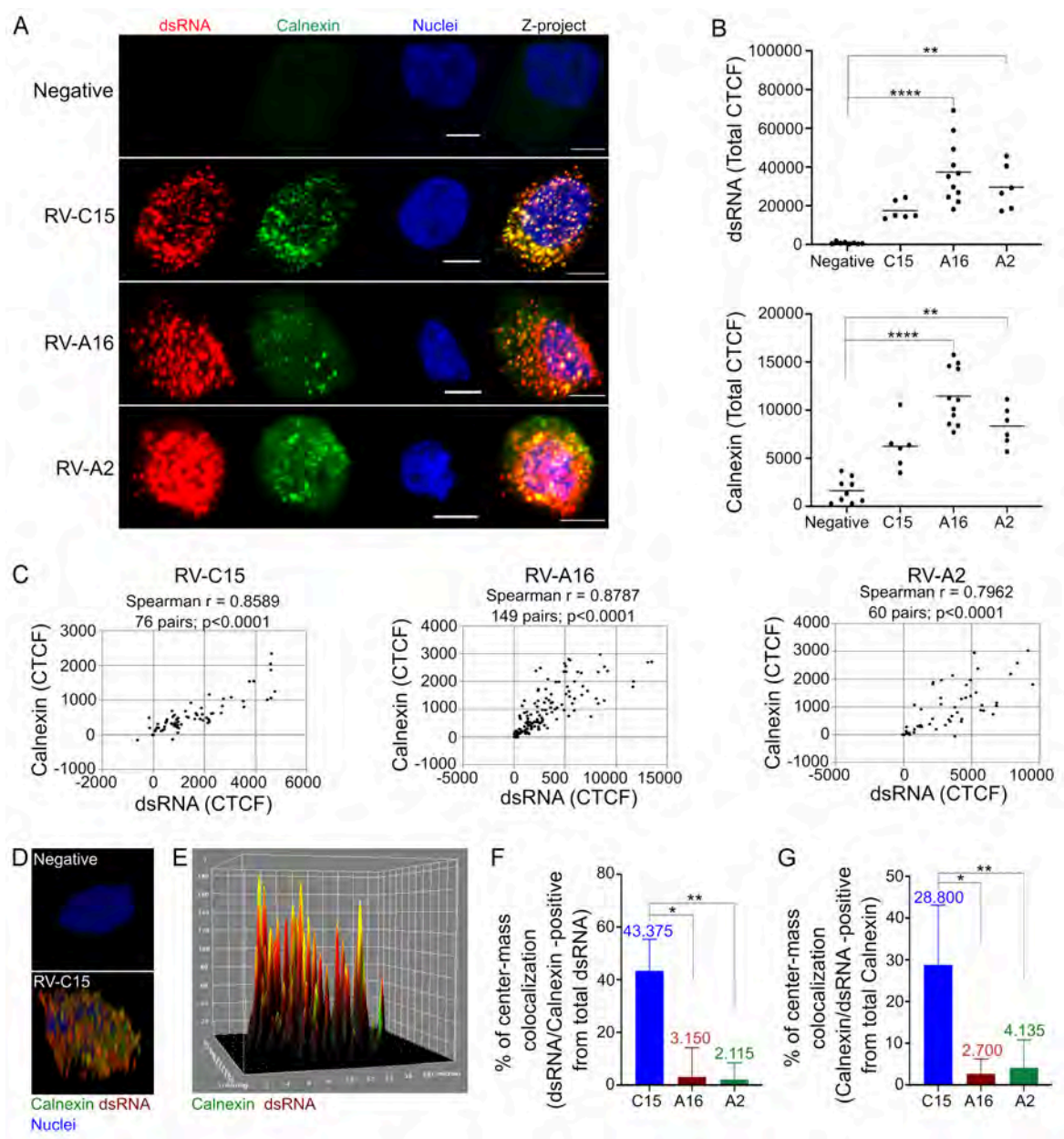
Figure 4. ER is a site for RV-C15 genome replication in HAE.
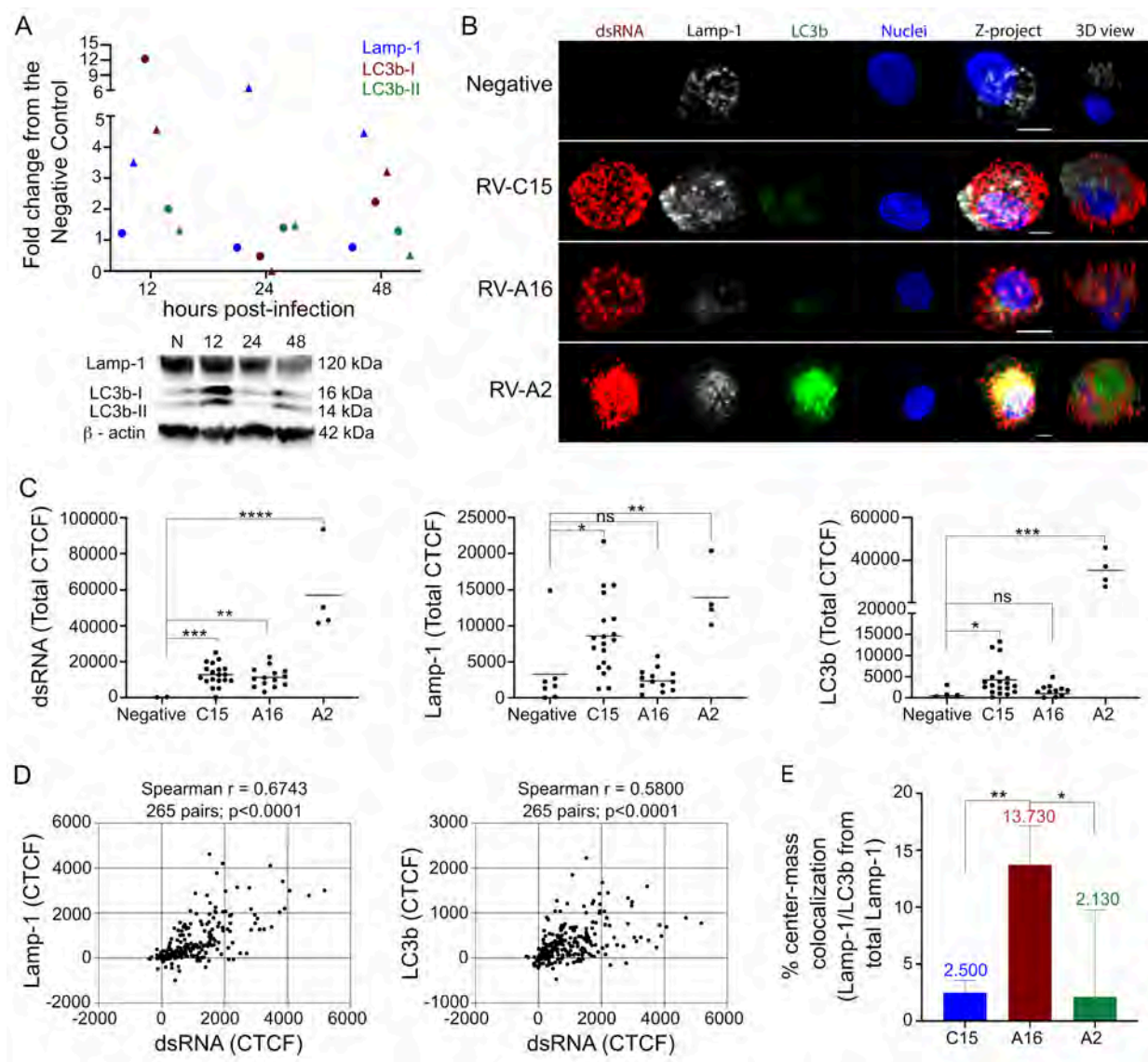
Figure 5. RV-C15 replication induces incomplete autophagy in HAE at 12 hpi.
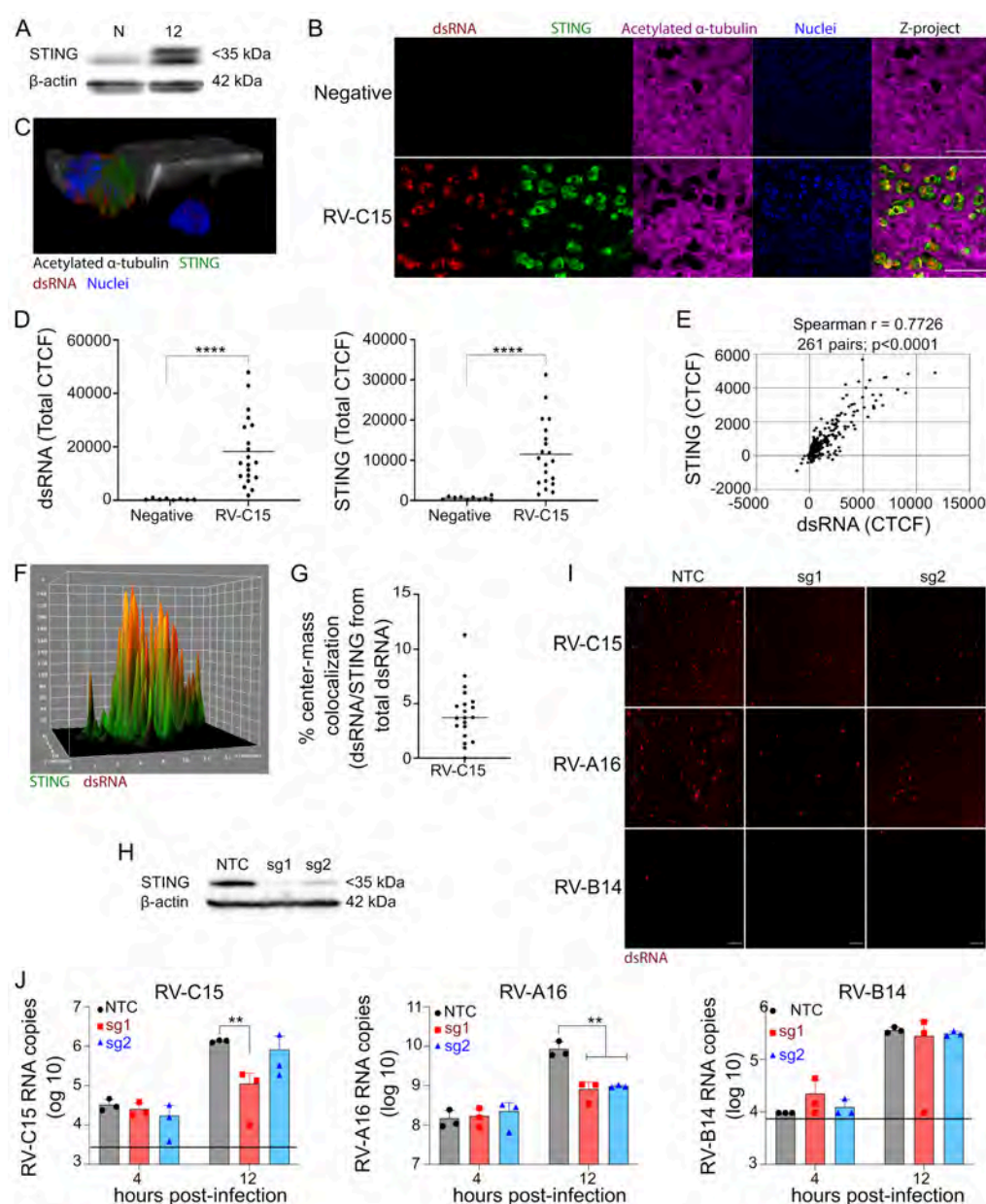
Figure 6. STING expression promotes RV-C15 replication in HAE at 12 hpi.

52
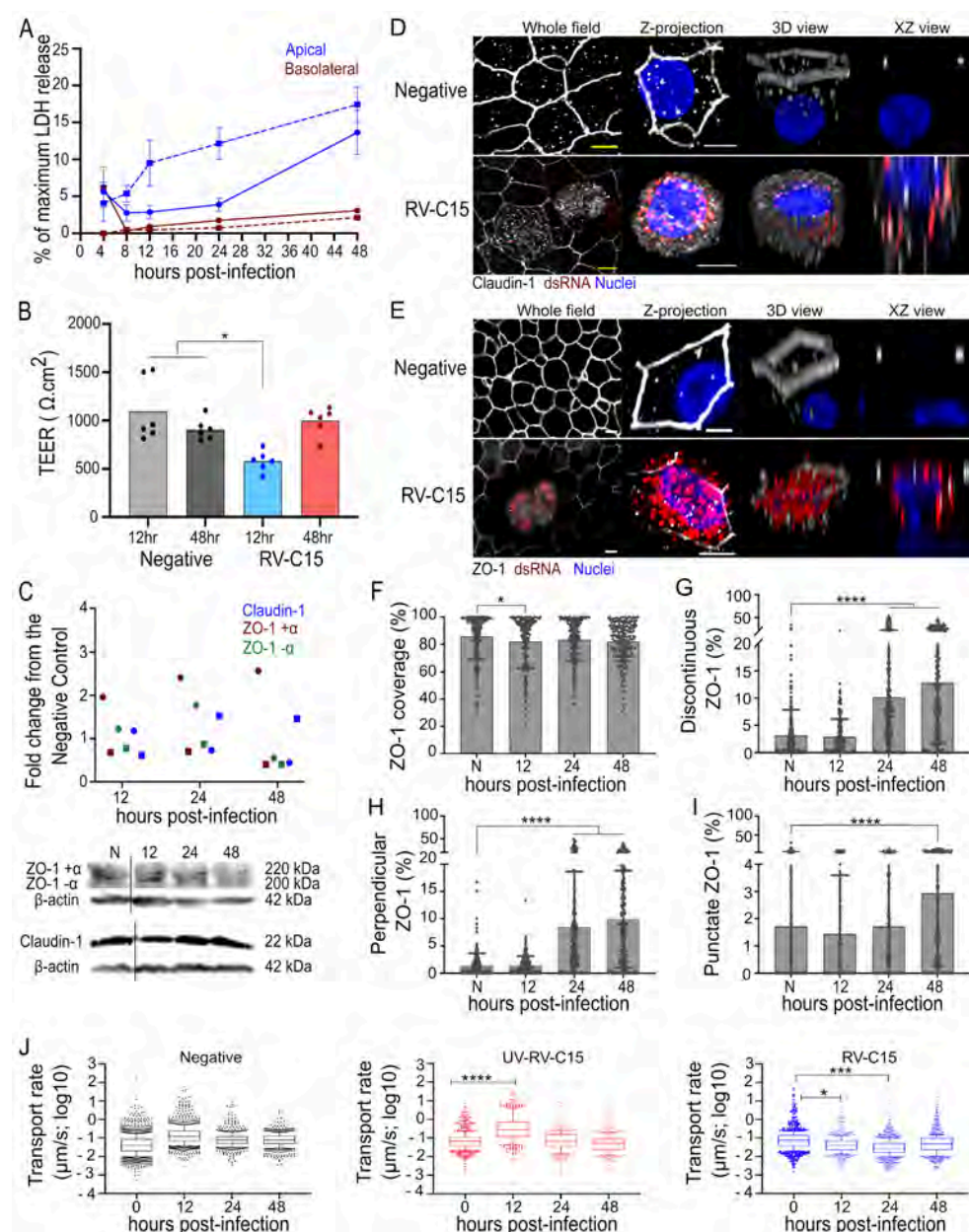
Figure 7. RV-C15 infection promotes translocation of tight junction proteins and impairs mucociliary clearance (MCC).

Supplementary files

I. Supplementary tables

S1 Table. Pixel-intensity based and spatial (distance between center-mass) colocalization analysis between giantin and PI4P in RV-C15 infected HAE.

Sample	PCC	thM1	thM2	Van Steensel's dx (pixel)	% center-mass colocalization (giantin/PI4P from total giantin)
RV-C15 1A	0.190	0.136	0.319	-1	3.45%
RV-C15 1B	0.106	0.071	0.264	1	3.63%
RV-C15 2A	0.188	0.148	0.206	2	7.37%
RV-C15 2B	0.251	0.299	0.265	2	8.93%
RV-C15 2C	0.080	0.105	0.085	0	4.21%
RV-C15 3A	0.305	0.226	0.459	0	11.46%
RV-C15 3B	0.228	0.233	0.267	-1	6.96%
RV-C15 4A	0.187	0.129	0.367	2	2.91%
RV-C15 4B	0.168	0.158	0.219	2	3.92%
RV-C15 4C	0.209	0.212	0.258	2	12.77%
RV-C15 4D	0.167	0.129	0.269	5	6.17%
RV-C15 4E	0.023	0.036	0.025	1	4.00%
RV-C15 4F	0.093	0.107	0.106	4	15.69%
RV-C15 5A	0.074	0.066	0.106	3	7.14%
RV-C15 5B	0.083	0.068	0.140	-5	5.48%
RV-C15 5C	0.092	0.122	0.082	1	9.52%
RV-C15 6A	0.232	0.190	0.316	0	9.84%
RV-C15 6B	0.099	0.131	0.087	3	8.33%
RV-C15 6C	0.150	0.152	0.161	-1	8.77%
Median	**0.167**	**0.131**	**0.219**	**1**	**7.14%**

S2 Table. Pixel-intensity based and spatial (distance between center-mass) colocalization analysis between giantin and PI4P in RV-A16 infected HAE.

Sample	PCC	thM1	thM2	Van Steensel's dx (pixel)	% center-mass colocalization (giantin/PI4P from total giantin)
RV-A16 1A	0.053	0.066	0.068	-15	3.45%
RV-A16 1B	0.133	0.083	0.266	-4	2.50%
RV-A16 1C	0.081	0.073	0.135	2	9.43%
RV-A16 2A	0.051	0.076	0.093	-17	3.75%
RV-A16 2B	0.102	0.095	0.150	9	0.00%
RV-A16 2C	0.062	0.049	0.109	1	2.22%
RV-A16 3A	0.206	0.166	0.328	-2	7.69%
RV-A16 3B	0.035	0.028	0.110	17	0.00%
RV-A16 3C	0.210	0.133	0.421	3	6.25%
RV-A16 3D	0.192	0.151	0.271	1	0.00%
RV-A16 4A	0.086	0.063	0.189	20	3.17%
RV-A16 4B	0.081	0.046	0.187	6	2.60%
RV-A16 4C	0.122	0.054	0.319	-2	4.11%
Median	**0.086**	**0.073**	**0.187**	**1**	**3.17%**

S3 Table. Pixel-intensity based and spatial (distance between center-mass) colocalization analysis between giantin and PI4P in RV-A2 infected HAE.

Sample	PCC	thM1	thM2	Van Steensel's dx (pixel)	% center-mass colocalization (giantin/PI4P from total giantin)
RV-A2 1A	0.141	0.165	0.136	2	16.67%
RV-A2 1B	0.116	0.125	0.122	4	6.00%
RV-A2 2A	0.066	0.059	0.113	2	2.19%
RV-A2 2B	0.206	0.216	0.231	-3	2.50%
RV-A2 3A	0.039	0.056	0.035	1	3.85%
RV-A2 4A	0.028	0.032	0.041	5	3.70%
RV-A2 5A	0.095	0.092	0.122	-1	7.14%
RV-A2 6A	0.180	0.279	0.158	0	5.26%
Median	**0.106**	**0.109**	**0.122**	**2**	**4.55%**

S4 Table. Pixel-intensity based and spatial (distance between center-mass) colocalization analysis between dsRNA and giantin in RV-C15 infected HAE.

Sample	PCC	thM1	thM2	Van Steensel's dx (pixel)	% center-mass colocalization (dsRNA/giantin from total dsRNA)
RV-C15 1A	0.174	0.157	0.228	-1	3.65%
RV-C15 1B	0.175	0.153	0.248	1	11.39%
RV-C15 2A	0.168	0.158	0.227	2	13.04%
RV-C15 2B	0.237	0.354	0.191	2	11.83%
RV-C15 2C	0.176	0.223	0.158	0	23.53%
RV-C15 3A	0.117	0.120	0.149	-1	14.85%
RV-C15 3B	0.133	0.167	0.142	2	5.62%
RV-C15 4A	0.094	0.125	0.102	1	8.43%
RV-C15 4B	0.142	0.122	0.215	1	11.11%
RV-C15 4C	0.150	0.165	0.187	8	12.90%
RV-C15 4D	0.106	0.124	0.117	1	5.36%
RV-C15 4E	0.105	0.080	0.168	0	2.02%
RV-C15 4F	0.056	0.069	0.071	2	11.46%
RV-C15 5A	0.062	0.044	0.128	-3	8.54%
RV-C15 5B	0.079	0.071	0.121	-7	2.47%
RV-C15 5C	0.102	0.083	0.162	-1	4.81%
RV-C15 6A	0.162	0.163	0.185	0	6.93%
RV-C15 6B	0.060	0.056	0.094	3	6.59%
RV-C15 6C	0.085	0.056	0.163	1	10.87%
Median	**0.117**	**0.124**	**0.162**	**1**	**8.54%**

S5 Table. Pixel-intensity based and spatial (distance between center-mass) colocalization analysis between dsRNA and giantin in RV-A16 infected HAE.

Sample	PCC	thM1	thM2	Van Steensel's dx (pixel)	% center-mass colocalization (dsRNA/giantin from total dsRNA)
RV-A16 1A	0.069	0.056	0.146	-12	6.67%
RV-A16 1B	0.133	0.092	0.235	0	5.47%
RV-A16 1C	0.069	0.055	0.147	2	3.96%
RV-A16 2A	0.140	0.128	0.241	0	3.41%
RV-A16 2B	0.050	0.049	0.104	1	4.65%
RV-A16 2C	0.032	0.023	0.097	0	5.08%
RV-A16 3A	0.161	0.173	0.194	-14	10.20%
RV-A16 3B	0.138	0.079	0.308	1	15.38%
RV-A16 3C	0.007	0.024	0.043	20	2.04%
RV-A16 3D	0.060	0.056	0.091	-9	5.13%
RV-A16 4A	0.105	0.122	0.116	4	6.48%
RV-A16 4B	0.004	0.010	0.018	15	2.22%
RV-A16 4C	0.074	0.045	0.149	-19	2.94%
Median	**0.069**	**0.056**	**0.146**	**0**	**5.08%**

S6 Table. Pixel-intensity based and spatial (distance between center-mass) colocalization analysis between dsRNA and giantin in RV-A2 infected HAE.

Sample	PCC	thM1	thM2	Van Steensel's dx (pixel)	% center-mass colocalization (dsRNA/giantin from total dsRNA)
RV-A2 1A	0.032	0.036	0.058	2	3.54%
RV-A2 1B	0.045	0.038	0.088	14	4.26%
RV-A2 2A	0.053	0.058	0.077	1	11.54%
RV-A2 2B	0.046	0.074	0.054	-19	5.15%
RV-A2 3A	0.044	0.029	0.108	1	1.30%
RV-A2 4A	0.087	0.066	0.140	0	8.62%
RV-A2 5A	0.075	0.046	0.190	19	7.50%
RV-A2 6A	0.106	0.179	0.110	10	5.21%
Median	**0.050**	**0.052**	**0.098**	**2**	**5.18%**

S7 Table. Pixel-intensity based and spatial (distance between center-mass) colocalization analysis between dsRNA and PI4P in RV-C15 infected HAE.

Sample	PCC	thM1	thM2	Van Steensel's dx (pixel)	% center-mass colocalization (dsRNA/PI4P from total dsRNA)
RV-C15 1A	0.259	0.357	0.220	0	4.38%
RV-C15 1B	0.108	0.224	0.098	-2	3.80%
RV-C15 2A	0.281	0.371	0.256	0	10.14%
RV-C15 2B	0.280	0.385	0.235	-1	4.30%
RV-C15 2C	0.051	0.068	0.060	-1	9.80%
RV-C15 3A	0.212	0.298	0.182	0	7.92%
RV-C15 3B	0.230	0.290	0.215	-1	4.49%
RV-C15 4A	0.253	0.519	0.148	0	19.28%
RV-C15 4B	0.227	0.220	0.280	-1	11.11%
RV-C15 4C	0.292	0.327	0.305	-1	19.35%
RV-C15 4D	0.244	0.388	0.176	0	2.54%
RV-C15 4E	0.040	0.029	0.087	-2	2.02%
RV-C15 4F	0.052	0.065	0.067	0	3.13%
RV-C15 5A	0.211	0.168	0.302	-2	7.32%
RV-C15 5B	0.092	0.122	0.101	-1	2.47%
RV-C15 5C	0.082	0.055	0.161	-1	3.85%
RV-C15 6A	0.295	0.371	0.254	0	7.92%
RV-C15 6B	0.144	0.097	0.243	0	8.79%
RV-C15 6C	0.130	0.085	0.233	6	10.87%
Median	**0.212**	**0.224**	**0.215**	**-1**	**7.32%**

S8 Table. Pixel-intensity based and spatial (distance between center-mass) colocalization analysis between dsRNA and PI4P in RV-A16 infected HAE.

Sample	PCC	thM1	thM2	Van Steensel's dx (pixel)	% center-mass colocalization (dsRNA/PI4P from total dsRNA)
RV-A16 1A	0.068	0.056	0.142	-1	6.67%
RV-A16 1B	0.105	0.146	0.117	1	3.97%
RV-A16 1C	0.194	0.184	0.262	-1	2.97%
RV-A16 2A	0.095	0.111	0.170	-1	0.00%
RV-A16 2B	0.099	0.108	0.144	0	4.65%
RV-A16 2C	0.048	0.052	0.098	0	3.39%
RV-A16 3A	0.243	0.359	0.204	2	6.12%
RV-A16 3B	0.116	0.154	0.154	-13	7.69%
RV-A16 3C	0.184	0.296	0.165	0	2.04%
RV-A16 3D	0.193	0.218	0.195	-1	6.41%
RV-A16 4A	0.196	0.382	0.122	0	2.78%
RV-A16 4B	0.112	0.192	0.084	0	2.22%
RV-A16 4C	0.201	0.290	0.163	2	5.88%
Median	**0.116**	**0.184**	**0.154**	**0**	**3.97%**

S9 Table. Pixel-intensity based and spatial (distance between center-mass) colocalization analysis between dsRNA and PI4P in RV-A2 infected HAE.

Sample	PCC	thM1	thM2	Van Steensel's dx (pixel)	% center-mass colocalization (dsRNA/PI4P from total dsRNA)
RV-A2 1A	0.072	0.060	0.118	-1	1.77%
RV-A2 1B	0.077	0.058	0.137	-2	3.19%
RV-A2 2A	0.110	0.152	0.106	-1	12.82%
RV-A2 2B	0.118	0.163	0.111	-1	6.19%
RV-A2 3A	0.049	0.024	0.141	-1	2.60%
RV-A2 4A	0.079	0.069	0.115	-2	4.31%
RV-A2 5A	0.081	0.058	0.182	0	5.63%
RV-A2 6A	0.211	0.224	0.243	-1	16.13%
Median	**0.080**	**0.065**	**0.128**	**-1**	**4.97%**

S10 Table. Pixel-intensity based and spatial (distance between center-mass) colocalization analysis between dsRNA and calnexin in RV-C15-infected HAE.

Sample	PCC	thM1	thM2	Van Steensel's dx (pixel)	% center-mass colocalization (dsRNA/calnexin from total dsRNA)
RVC15_1A	0.53	0.63	0.47	2	54.93%
RVC15_1B	0.49	0.51	0.49	2	41.67%
RVC15_2C	0.19	0.13	0.34	1	4.38%
RVC15_2D	0.41	0.6	0.29	2	28.77%
RVC15_3E	0.29	0.55	0.16	1	45.08%
RVC15_4F	0.35	0.57	0.22	1	55.36%
Median	**0.381**	**0.563**	**0.317**	**1.5**	**43.37%**

S11 Table. Pixel-intensity based and spatial (distance between center-mass) colocalization analysis between dsRNA and calnexin in RV-A16-infected HAE.

Sample	PCC	thM1	thM2	Van Steensel's dx (pixel)	% center-mass colocalization (dsRNA/calnexin from total dsRNA)
RV-A16_1A	0.366	0.407	0.387	1	14.18%
RV-A16_1B	0.289	0.372	0.292	3	10.16%
RV-A16_1C	0.265	0.328	0.271	2	2.97%
RV-A16_1D	0.340	0.231	0.607	3	2.68%
RV-A16_1E	0.287	0.276	0.374	2	3.26%
RV-A16_2F	0.352	0.263	0.618	2	3.15%
RV-A16_2G	0.320	0.236	0.584	4	0.83%
RV-A16_2H	0.358	0.255	0.637	3	0.55%
RV-A16_3I	0.339	0.389	0.359	2	22.35%
RV-A16_3J	0.272	0.315	0.312	2	1.05%
RV-A16_3K	0.364	0.280	0.633	0	4.04%
Median	**0.339**	**0.280**	**0.387**	**2**	**3.15%**

S12 Table. Pixel-intensity based and spatial (distance between center-mass) colocalization analysis between dsRNA and calnexin in RV-A2-infected HAE.

Sample	PCC	thM1	thM2	Van Steensel's dx (pixel)	% center-mass colocalization (dsRNA/calnexin from total dsRNA)
RV-A2_1A	0.3	0.5	0.22	2	1.79%
RV-A2_2B	0.37	0.58	0.29	-1	8.42%
RV-A2_3C	0.43	0.51	0.44	2	1.56%
RV-A2_4D	0.45	0.48	0.52	2	1.73%
RV-A2_6E	0.33	0.47	0.29	2	2.44%
RV-A2_7A	0.28	0.48	0.22	1	2.58%
Median	**0.353**	**0.491**	**0.288**	**2**	**2.11%**

S13 Table. Pixel-intensity based and spatial (distance between center-mass) colocalization analysis between dsRNA and giantin in RV-C15- infected HAE.

Sample	PCC	thM1	thM2	Van Steensel's dx (pixel)	% center-mass colocalization (dsRNA/giantin from total dsRNA)
RVC15_1A	0.14	0.15	0.15	-1	18.31%
RVC15_1B	0.19	0.2	0.2	-3	12.50%
RVC15_2C	0.07	0.06	0.15	1	2.51%
RVC15_2D	0.13	0.2	0.1	0	10.96%
RVC15_3E	0.09	0.17	0.06	-2	24.59%
RVC15_4F	0.15	0.23	0.11	-1	25.23%
Median	**0.136**	**0.183**	**0.130**	**-1**	**15.40%**

S14 Table. Pixel-intensity based and spatial (distance between center-mass) colocalization analysis between dsRNA and giantin in RV-A16-infected HAE.

Sample	PCC	thM1	thM2	Van Steensel's dx (pixel)	% center-mass colocalization (dsRNA/giantin from total dsRNA)
RV-A16_1A	0.372	0.501	0.333	-3	10.64%
RV-A16_1B	0.331	0.441	0.313	2	1.56%
RV-A16_1C	0.363	0.607	0.264	-1	6.93%
RV-A16_1D	0.241	0.306	0.311	1	0.24%
RV-A16_1E	0.269	0.480	0.223	-1	14.67%
RV-A16_2F	0.319	0.346	0.450	-1	2.45%
RV-A16_2G	0.376	0.378	0.515	5	3.32%
RV-A16_2H	0.241	0.318	0.337	0	0.00%
RV-A16_3I	0.115	0.172	0.153	0	8.24%
RV-A16_3J	0.215	0.311	0.228	5	21.05%
RV-A16_3K	0.259	0.260	0.440	-18	1.01%
Median	**0.269**	**0.346**	**0.313**	**0**	**3.32%**

S15 Table. Pixel-intensity based and spatial (distance between center-mass) colocalization analysis between dsRNA and giantin in RV-A2- infected HAE.

Sample	PCC	thM1	thM2	Van Steensel's dx (pixel)	% center-mass colocalization (dsRNA/giantin from total dsRNA)
RV-A2_1A	0.19	0.27	0.21	0	4.11%
RV-A2_2B	0.33	0.52	0.27	-3	2.11%
RV-A2_3C	0.27	0.3	0.33	2	1.56%
RV-A2_4D	0.34	0.36	0.44	0	8.67%
RV-A2_6E	0.26	0.39	0.23	-1	7.32%
RV-A2_7A	0.22	0.39	0.18	1	2.58%
Median	**0.266**	**0.378**	**0.249**	**0**	**3.35%**

9

S16 Table. Pixel-intensity based and spatial (distance between center-mass) colocalization analysis between dsRNA and STING in RV-C15-infected HAE.

| Sample	PCC	thM1	thM2	Van Steensel's dx (pixel)	% center-mass colocalization (dsRNA/STING from total dsRNA)
RVC15_1A	0.241	0.256	0.288	0	3.74%
RVC15_1B	0.363	0.492	0.326	2	0.92%
RVC15_1C	0.297	0.207	0.597	-4	11.25%
RVC15_1D	0.025	0.029	0.054	2	6.00%
RVC15_1E	0.055	0.055	0.090	3	3.68%
RVC15_1F	0.041	0.044	0.087	0	2.97%
RVC15_1G	0.060	0.030	0.163	-2	1.32%
RVC15_1H	0.005	0.023	0.021	-1	1.46%
RVC15_2A	0.321	0.406	0.319	-1	7.55%
RVC15_2B	0.367	0.395	0.455	-1	6.56%
RVC15_2C	0.239	0.197	0.333	2	2.90%
RVC15_2D	0.212	0.232	0.300	-7	3.70%
RVC15_2E	0.005	0.021	0.049	-3	5.17%
RVC15_2F	0.127	0.096	0.213	-1	4.65%
RVC15_3A	0.402	0.471	0.400	2	4.76%
RVC15_3B	0.314	0.268	0.466	-3	2.04%
RVC15_3C	0.265	0.266	0.325	0	3.28%
RVC15_3D	0.198	0.152	0.300	1	4.94%
RVC15_3E	0.455	0.631	0.371	1	0.00%
RVC15_3F	0.149	0.292	0.101	1	4.29%
Median	**0.226**	**0.220**	**0.300**	**0**	**3.72%**

S17 Table. Pixel-intensity based and spatial (distance between center-mass) colocalization analysis between Lamp1 and LC3b in RV-C15-infected HAE.

| Sample	PCC	thM1	thM2	Van Steensel's dx (pixel)	% center-mass colocalization (Lamp1/LC3b from total Lamp1)
RV-C15-1A	0.262	0.129	0.570	-1	5.17%
RV-C15-1B	0.040	0.032	0.098	-1	1.43%
RV-C15-1C	0.159	0.114	0.300	0	3.57%
RV-C15-1D	0.048	0.016	0.240	0	0.00%
RV-C15-2A	0.058	0.034	0.183	-2	4.55%
RV-C15-2B	0.256	0.120	0.631	-1	16.67%
RV-C15-2C	0.027	0.016	0.107	-1	0.00%
RV-C15-3A	0.148	0.037	0.684	-1	0.00%
RV-C15-3B	0.157	0.047	0.620	-1	3.06%
RV-C15-3C	0.107	0.023	0.596	-2	12.50%
RV-C15-3D	0.186	0.071	0.577	-2	3.13%
RV-C15-4A	0.128	0.030	0.677	-2	2.50%
RV-C15-4B	0.142	0.040	0.597	-2	0.00%
RV-C15-4C	0.186	0.061	0.690	-3	2.50%
RV-C15-5A	0.249	0.082	0.792	-1	2.60%
RV-C15-5B	0.067	0.010	0.534	-1	0.00%
RV-C15-6A	0.321	0.153	0.723	-1	3.13%
RV-C15-6B	0.054	0.012	0.323	0	0.00%
RV-C15-6C	0.024	0.007	0.129	-1	0.00%
Median	**0.142**	**0.037**	**0.577**	**-1**	**2.50%**

S18 Table. Pixel-intensity based and spatial (distance between center-mass) colocalization analysis between Lamp1 and LC3b in RV-A16-infected HAE.

Sample	PCC	thM1	thM2	Van Steensel's dx (pixel)	% center-mass colocalization (Lamp1/LC3b from total Lamp1)
RV-A16-1A	0.604	0.670	0.569	-1	16.67%
RV-A16-1B	0.388	0.585	0.296	-1	9.38%
RV-A16-1C	0.399	0.635	0.290	-2	0.00%
RV-A16-3A	0.510	0.610	0.488	-1	24.14%
RV-A16-3B	0.435	0.584	0.356	-1	17.07%
RV-A16-3C	0.409	0.557	0.338	-2	8.33%
RV-A16-3D	0.583	0.665	0.538	-2	27.27%
RV-A16-4A	0.568	0.647	0.530	-1	16.67%
RV-A16-4C	0.535	0.618	0.493	-1	7.41%
RV-A16-5A	0.395	0.590	0.308	-2	13.73%
RV-A16-5B	0.418	0.605	0.318	-2	2.86%
RV-A16-5C	0.392	0.599	0.304	-2	17.14%
RV-A16-5D	0.456	0.639	0.376	-2	7.32%
Median	**0.435**	**0.610**	**0.356**	**-2**	**13.73%**

S19 Table. Pixel-intensity based and spatial (distance between center-mass) colocalization analysis between Lamp 1 and LC3b in RV-A2-infected HAE.

| Sample	PCC	thM1	thM2	Van Steensel's dx (pixel)	% center-mass colocalization (Lamp1/LC3b from total Lamp1)
RV-A2-1A	0.361	0.372	0.388	0	9.76%
RV-A2-2A	0.370	0.175	0.869	-1	2.13%
RV-A2-3A	0.393	0.281	0.601	-1	3.80%
RV-A2-3B	0.228	0.225	0.299	0	0.00%
RV-A2-4A	0.166	0.096	0.367	-2	0.00%
RV-A2-4b	0.141	0.119	0.231	-2	0.00%
RV-A2-4C	0.135	0.120	0.242	-3	4.08%
Median	**0.228**	**0.175**	**0.367**	**-1**	**2.13%**

## II. Supplementary figures
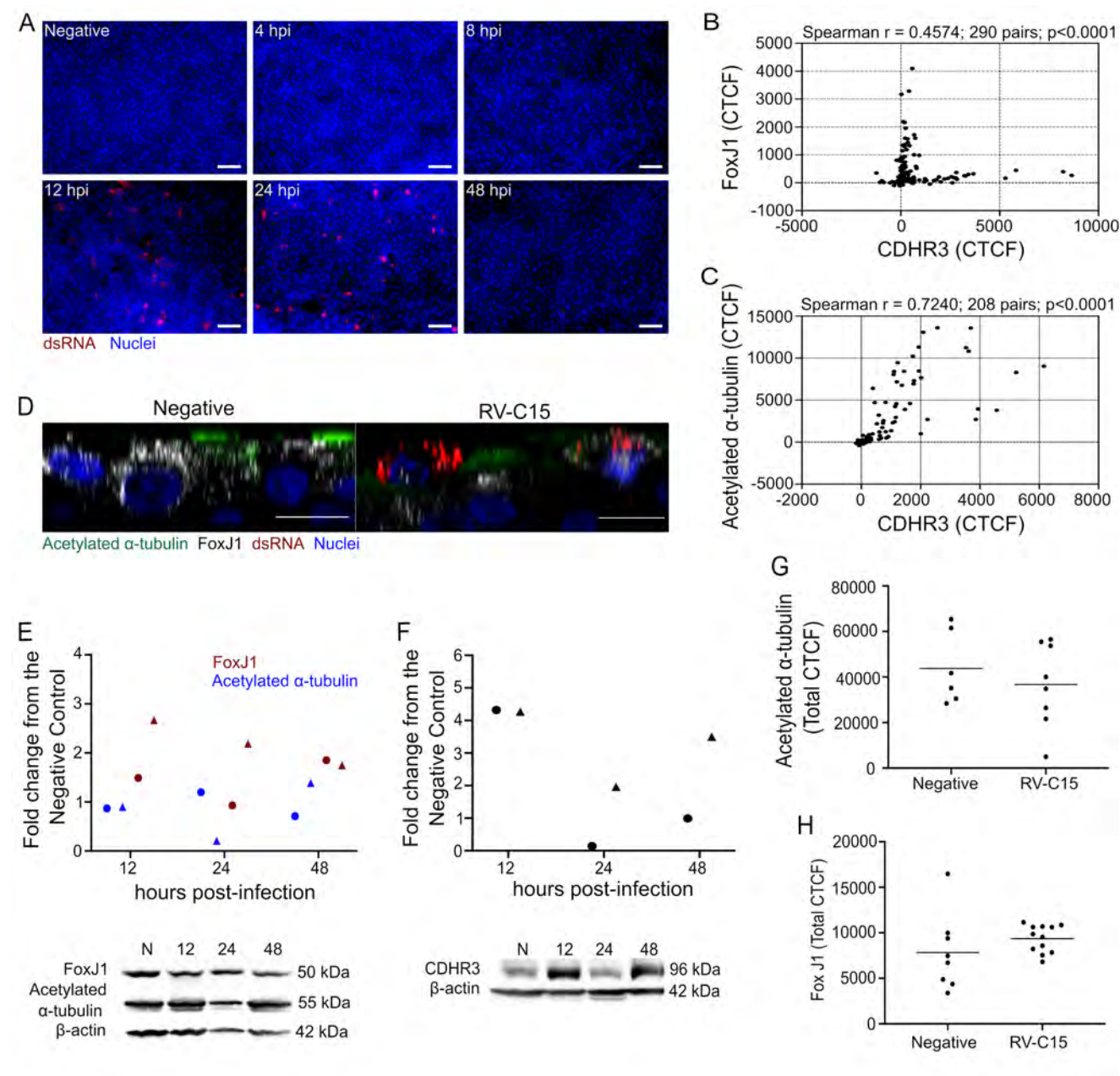
S1 Figure. RV-C15 replicates in ciliated epithelial cells, leading to decreased CDHR3 levels.
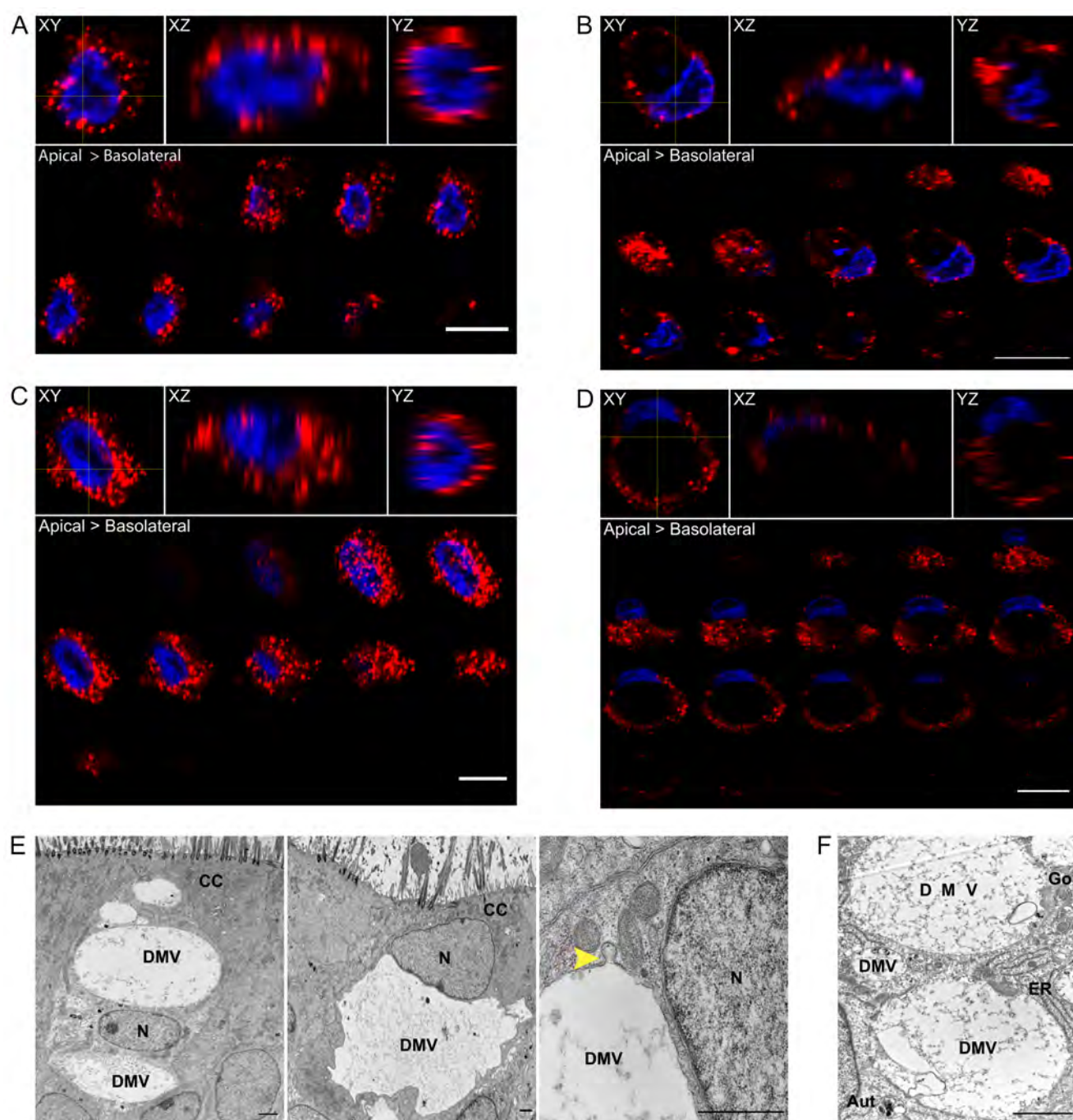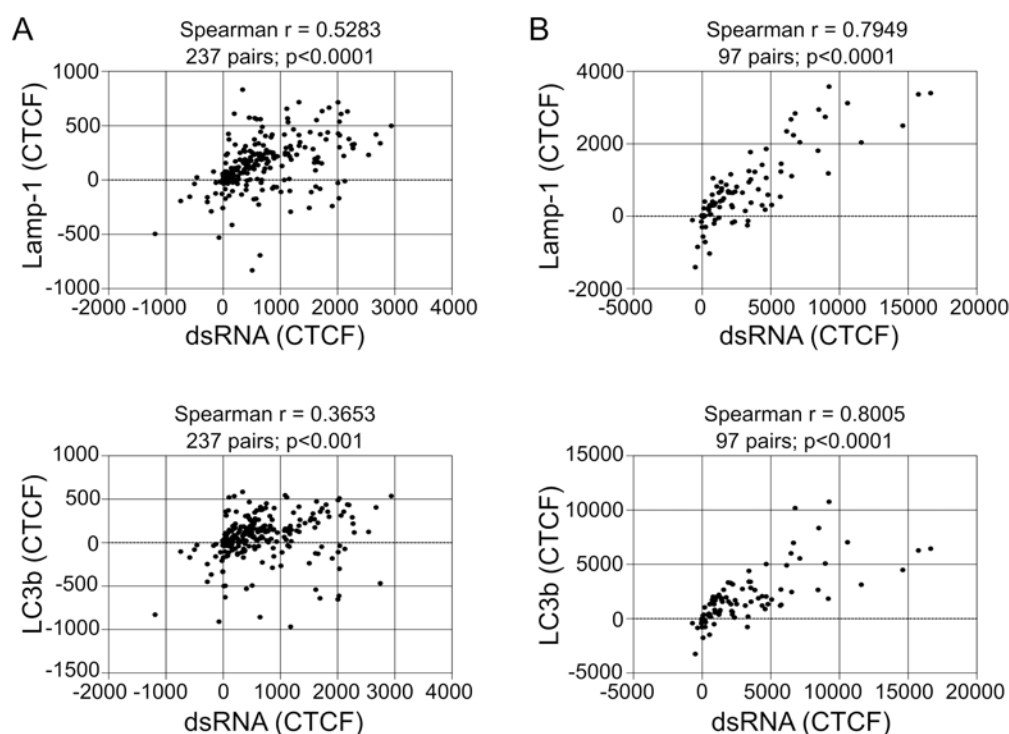
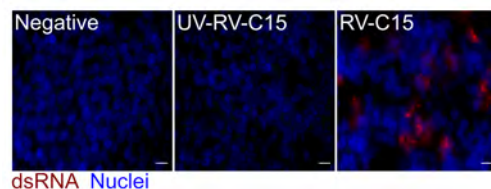**S2 Figure. "Ring-like" dsRNA localization in HAE is not specific to RV-C15 infection.**
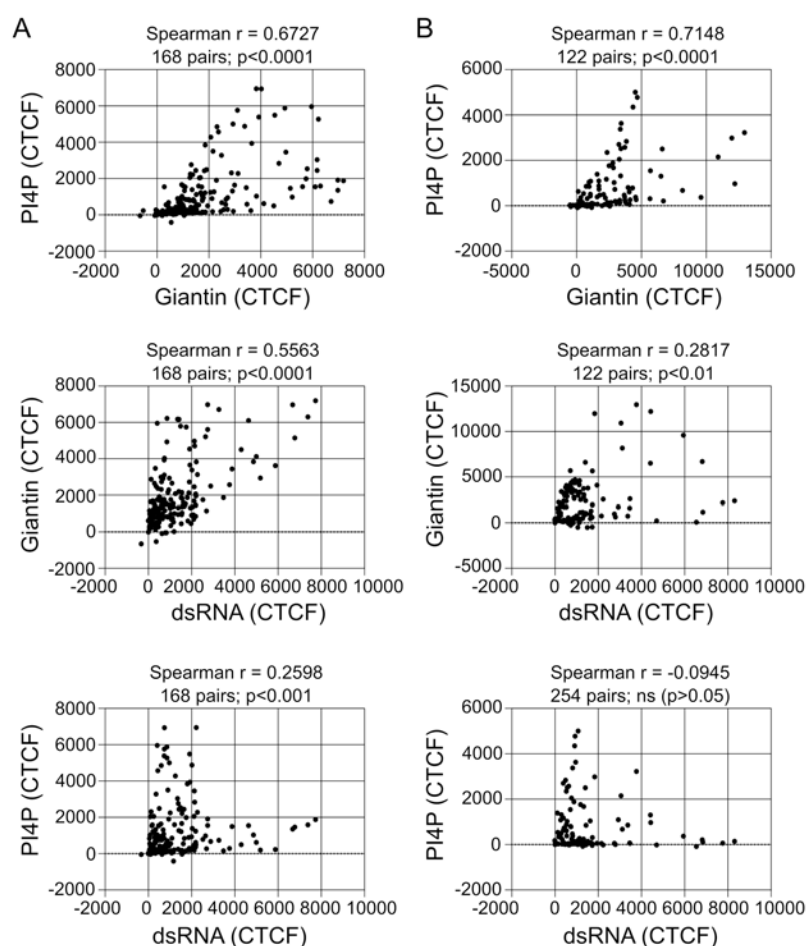
S3 Figure. Neither the Golgi nor PI4P-positive vesicles are the main site for RV-C15 replication in HAE.

S4 Figure. Global calnexin expression is not altered during RV-C15 infection in HAE.

15
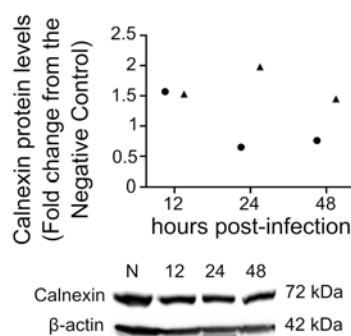
S5 Figure. RV-C15 replication induces incomplete autophagy in HAE at 12 hpi.

S6 Figure. Detection of dsRNA in RV-C15, but not UV-RV-C15, inoculated HAE used in the MCC experiment.